



Understanding the Broad-line Region of Active Galactic Nuclei with Photoionization. I. The Moderate-accretion Regime

Qiaoya Wu¹, Yue Shen^{1,2}, Hengxiao Guo³, Scott F. Anderson⁴, W. N. Brandt^{5,6,7}, Catherine J. Grier⁸, Patrick B. Hall⁹, Luis C. Ho^{10,11}, Yasaman Homayouni^{5,12}, Keith Horne¹³, Jennifer I-Hsiu Li^{14,15}, and Donald P. Schneider^{5,6}

¹ Department of Astronomy, University of Illinois at Urbana-Champaign, Urbana, IL 61801, USA; qiaoyaw2@illinois.edu, shenyue@illinois.edu

² National Center for Supercomputing Applications, University of Illinois at Urbana-Champaign, Urbana, IL 61801, USA

³ Shanghai Astronomical Observatory, Chinese Academy of Sciences, 80 Nandan Road, Shanghai 200030, People's Republic of China

⁴ Astronomy Department, University of Washington, Box 351580, Seattle, WA 98195, USA

⁵ Department of Astronomy and Astrophysics, The Pennsylvania State University, University Park, PA 16802, USA

⁶ Institute for Gravitation and the Cosmos, The Pennsylvania State University, University Park, PA 16802, USA

⁷ Department of Physics, 104 Davey Laboratory, The Pennsylvania State University, University Park, PA 16802, USA

⁸ Department of Astronomy, University of Wisconsin–Madison, Madison, WI 53706, USA

⁹ Department of Physics and Astronomy, York University, 4700 Keele Street, Toronto, ON M3J 1P3, Canada

¹⁰ Kavli Institute for Astronomy and Astrophysics, Peking University, Beijing 100871, People's Republic of China

¹¹ Department of Astronomy, School of Physics, Peking University, Beijing 100871, People's Republic of China

¹² Space Telescope Science Institute, 3700 San Martin Drive, Baltimore, MD 21218, USA

¹³ SUPA Physics and Astronomy, University of St Andrews, Fife, KY16 9SS, UK

¹⁴ Michigan Institute for Data Science, University of Michigan, Ann Arbor, MI 48109, USA

¹⁵ Department of Astronomy, University of Michigan, Ann Arbor, MI 48109, USA

Received 2024 July 1; revised 2024 December 4; accepted 2024 December 25; published 2025 February 7

Abstract

Over three decades of reverberation mapping (RM) studies on local broad-line active galactic nuclei (AGNs) have measured reliable black hole (BH) masses for >100 AGNs. These RM measurements reveal a significant correlation between the Balmer broad-line region (BLR) size and AGN optical luminosity (the R – L relation). Recent RM studies for AGN samples with more diverse BH parameters (e.g., mass and Eddington ratio) reveal a substantial intrinsic dispersion around the average R – L relation, suggesting that variations in the broadband spectrum, driven by accretion parameters and other factors such as the cloud distribution and inclination, significantly influence the measured R – L relation. Here we perform a detailed photoionization investigation of expected broad-line properties as functions of accretion parameters using AGN continuum models from `qsosed`. We compare theoretical predictions with observations of a sample of 67 $z \lesssim 0.5$ reverberation-mapped AGNs with rest-frame optical and UV spectra in the moderate-accretion regime (Eddington ratio $\lambda_{\text{Edd}} \equiv L/L_{\text{Edd}} < 0.5$). The UV/optical line strengths and their dependences on accretion parameters are reasonably well reproduced by the locally optimally emitting cloud photoionization models. We provide quantitative recipes using optical/UV line flux ratios to infer the unobservable ionizing continuum. Additionally, photoionization models with universal values of ionization parameter ($\log U_{\text{H}} = -2$) and hydrogen density ($\log n(\text{H}) = 12$) can qualitatively reproduce the observed global R – L relation for the current RM AGN sample. However, such models fail to reproduce the observed decrease in BLR size with increasing L/L_{Edd} at fixed optical luminosity, implying that gas density or BLR structure may systematically change with accretion rate.

Unified Astronomy Thesaurus concepts: Black hole physics (159); Quasars (1319); Active galactic nuclei (16)

1. Introduction

Reverberation mapping (RM) is a well-demonstrated technique to measure the black hole (BH) masses in active galactic nuclei (AGNs), using the distance and kinematics of the broad-line region (BLR) clouds. After several decades of RM work by different groups, there are now more than 100 local AGNs ($z \lesssim 0.3$) that have successful mass measurements with $H\beta$ RM (e.g., R. D. Blandford & C. F. McKee 1982; B. M. Peterson 1993; B. M. Peterson et al. 1998, 2002, 2004; S. Kaspi et al. 2007; A. J. Barth et al. 2015; P. Du et al. 2015; P. Du et al. 2018; C. Hu et al. 2021; V. U et al. 2022; U. Malik et al. 2023; S. Wang & J.-H. Woo 2024; J.-H. Woo et al. 2024). Recent dedicated RM programs are

also pushing these measurements to higher redshifts and to cover additional broad lines such as C IV and Mg II (P. Lira et al. 2018; C. J. Grier et al. 2019; J. K. Hoormann et al. 2019; Y. Homayouni et al. 2020; S. Kaspi et al. 2021; Z. Yu et al. 2021; U. Malik et al. 2023). Earlier studies on nearby RM AGNs have revealed a tight (i.e., scatter $\lesssim 0.15$ dex in BLR size) correlation between the average distance from the BH to $H\beta$ -emitting BLR clouds and the optical luminosity λL_{5100} of the AGN, known as the radius–luminosity (R – L) relation (S. Kaspi et al. 2000, 2007; M. C. Bentz et al. 2013):

$$\log(R_{\text{BLR}}/\text{lt} - \text{days}) = \alpha \log(\lambda L_{5100}/10^{44} \text{erg s}^{-1}) + \beta, \quad (1)$$

where M. C. Bentz et al. (2013) measured the slope $\alpha = 0.533^{+0.533}_{-0.033}$ and the intercept $\beta = 1.527 \pm 0.031$ at $\log(\lambda L_{5100}/\text{erg s}^{-1}) = 44$. This R – L relation provides the foundation for the so-called single-epoch virial BH mass

recipes (M. Vestergaard & B. M. Peterson 2006; Y. Shen 2013) that use a single monochromatic continuum luminosity to estimate the time lag. Due to their simplicity, these single-epoch BH mass recipes have been widely adopted to estimate BH masses in high-redshift quasars and for large AGN samples with single-epoch spectra (e.g., Y. Shen et al. 2011; Q. Wu & Y. Shen 2022). Furthermore, this tight local $R-L$ relation motivates its potential utility as a standard candle to measure luminosity distances for cosmology (D. Watson et al. 2011; M. L. Martínez-Aldama et al. 2019), once the BLR size is measured directly via RM.

However, recent RM studies targeting AGNs across broad ranges of luminosities and Eddington ratios have found evidence for increased dispersion around the canonical $R-L$ relation (e.g., P. Du et al. 2014; C. J. Grier et al. 2017; G. Fonseca Alvarez et al. 2020; Y. Shen et al. 2024). In particular, the super-Eddington accreting massive BH (SEAMBH) collaboration (P. Du et al. 2014, 2015; P. Du et al. 2018; C. Hu et al. 2021) and the Seoul National University AGN monitoring project (S. Wang & J.-H. Woo 2024; J.-H. Woo et al. 2024) targeting high-accretion-rate AGNs have found a surprising downward offset of the average $H\beta$ lag from the canonical relation in these objects. This suggests that variations in the accretion parameters (mass, accretion rate, and BH spin), along with factors like cloud distribution geometry and inclination (resulting in the transfer function of RM), significantly influence the observed distribution around the mean $R-L$ relation. The recent dynamical mass measurement of SDSS J092034.17+065718.0 ($z \approx 2.3$) from GRAVITY+ also reported a smaller BLR size than predicted by the canonical $R-L$ relation for this super-Eddington accretion quasar (R. Abuter et al. 2024). This spectro-interferometric method independently confirms that super-Eddington AGNs may have smaller BLR sizes as measured from RM. Meanwhile, the Sloan Digital Sky Survey RM (SDSS-RM) project (Y. Shen et al. 2015a, 2024; M. R. Blanton et al. 2017) targeting nonlocal AGNs at $0.1 < z < 4.5$ also found a large dispersion of ~ 0.3 dex around the mean $H\beta$ $R-L$ relation.

This increased scatter in the $R-L$ relation has gained significant interest in recent work (B. Czerny et al. 2019; P. Du & J.-M. Wang 2019; E. Dalla Bontà et al. 2020; G. Fonseca Alvarez et al. 2020). Understanding the origin of this dispersion and deriving corrections to potentially “tighten” the $R-L$ relation would have tremendous value both in designing better single-epoch mass recipes and in using the $R-L$ relation as a luminosity indicator. Detailed cadence and duration simulations of RM monitoring have ruled out selection bias as a major contributor to the observed scatter (I.-H. Li et al. 2019; G. Fonseca Alvarez et al. 2020). Several recent works have attempted to use the optical Fe II strength (denoted by $R_{\text{Fe II}} \equiv \text{EW}_{\text{Fe II}, 4434-4684} / \text{EW}_{\text{H}\beta}$) as a proxy to correct this offset (e.g., P. Du & J.-M. Wang 2019; M. L. Martínez-Aldama et al. 2019; L.-M. Yu et al. 2020; J. Maithil et al. 2022; Z. Yu et al. 2023), where $R_{\text{Fe II}}$ is considered a proxy of the Eddington ratio through the eigenvector 1 relations (T. A. Boroson & R. F. Green 1992; Y. Shen & L. C. Ho 2014). Meanwhile, S. Wang & J.-H. Woo (2024) also suggest that [O III] 5007 luminosity could potentially eliminate the offset between low-Eddington and high-Eddington objects, as $L_{[\text{O III}] 5007}$ systematically traces the Eddington ratio.

In this work, we consider the standard scenario that the BLR emission is sensitive to the ionizing continuum, which depends on the accretion rate and, consequently, the structure of the accretion flow. Accretion flows around BHs can be classified into three main regimes based on their accretion rates (here we use the dimensionless Eddington ratio $\lambda_{\text{Edd}} \equiv L_{\text{bol}}/L_{\text{Edd}} = L_{\text{bol}}/(1.26 \times 10^{38} M_{\text{BH}}/M_{\odot})$). First, at low-to-moderate accretion rates ($\lambda_{\text{Edd}} \lesssim 0.5$), the accretion flow can be reasonably modeled by the geometrically thin Shakura–Sunyaev disk (SSD; N. I. Shakura & R. A. Sunyaev 1973), where the optically thick gas radiates multitemperature blackbody radiation. As the accretion rate substantially increases to $\lambda_{\text{Edd}} \gtrsim 1$, the structure of the accretion flow undergoes significant transformations due to increased radiation pressure, leading to a slim disk (M. A. Abramowicz et al. 1988) where the disk height becomes comparable to the disk radius. Many of the high-Eddington-ratio AGNs included in the SEAMBH sample likely are better described by this slim disk model (P. Du et al. 2014). Conversely, at very low accretion rates ($\lambda_{\text{Edd}} < 10^{-3}$), the viscously dissipated energy heats the flow rather than being radiated away, resulting in an optically thin, hot advection-dominated accretion flow (F. Yuan & R. Narayan 2014). Recognizing that the BH accretion rate in different regimes can lead to dramatic changes in the accretion-flow geometry and the resulting shape of the spectral energy distribution (SED; e.g., L. C. Ho 2008; N. Castelló-Mor et al. 2016), and given that the exact transition λ_{Edd} between different disk geometry remains uncertain, we focus on AGNs with low-to-moderate accretion rates ($10^{-3} < \lambda_{\text{Edd}} < 0.5$), where the accretion flow is predominately in the SSD regime. However, contributions from the hot corona (and a potential warm corona) are also included in the model continuum SEDs (see Section 2.1 for details).

To fully understand the connection between the underlying ionizing continuum and observables, detailed photoionization calculations are required. In this work, we construct a series of SEDs and photoionization calculations to compare with the average $H\beta$ emission distance from RM and the observed quasar spectral properties. In Section 2, we describe our theoretical models for the AGN SEDs and our photoionization calculations using the locally optimally emitting cloud (LOC) model (J. Baldwin et al. 1995). In Section 3, we present our analysis of the observational data and comparison with the theoretical framework. We discuss our results in Section 4 and conclude in Section 5. Throughout this paper, we adopt a flat Λ CDM cosmology with $\Omega_M = 0.3$ and $H_0 = 70 \text{ km s}^{-1} \text{ Mpc}^{-1}$.

2. Theoretical Framework

A physically motivated photoionization model for the AGN BLR is the LOC model (J. Baldwin et al. 1995). This model assumes an axisymmetric distribution of continuous clouds with varying gas densities and distances from the central continuum source. The observed line emission is the collection of all illuminated clouds but is dominated by those with the highest efficiency of reprocessing the incident ionizing continuum. In the following section, we apply the LOC model to a series of SEDs with different BH parameters (mass and accretion rate) to predict broad-emission-line properties with photoionization calculations.

2.1. AGN SEDs with XSPEC

To generate a grid of ionizing SEDs with various BH parameters, we use the q_{sosed} (A. Kubota & C. Done 2018) model in XSPEC (K. A. Arnaud 1996) that has three featured components: a truncated standard thin-disk component providing multitemperature blackbody radiation, a hot Comptonized corona for nonthermal power-law emission dominating the X-ray continuum above 1 keV, and a soft X-ray excess from an intermediate warm Comptonizing component. Compared to its predecessor OPTXAGNF (C. Done et al. 2012), which assumes a single Comptonization spectrum for the seed photon energy due to the lack of interstellar absorption observations, the updated, physically driven model q_{sosed} treats the warm Comptonization component more carefully and assumes that the seed photon energy originates from the underlying cool material in the midplane (A. Kubota & C. Done 2018). Both S. Panda et al. (2019) and G. J. Ferland et al. (2020) utilize the q_{sosed} model in their BLR photoionization computations to explore the impact of the Eddington ratio on the BLR photoionization and demonstrate consistent results with observations. Moreover, comparison with the stacked AGN spectra shows that the q_{sosed} -predicted SEDs align well with intermediate BH masses in the range of $7.5 < \log M_{\text{BH}} < 9.0$ while showing a discrepancy with observations at optical/EUV for both ends (J. A. J. Mitchell et al. 2023). The uncertainties and limitations of q_{sosed} will be further discussed in Section 4.4. The q_{sosed} model fixes several disk parameters and includes reprocessing; the free input parameters are the BH mass (M_{BH}), the comoving distance from the object to the observer (D_c), the Eddington-scaled accretion rate ($\dot{m} \equiv \dot{M}/\dot{M}_{\text{Edd}} = \eta \dot{M} c^2 / L_{\text{Edd}}$, where η is the spin-dependent radiative efficiency, fixed at 0.057 for a nonspinning BH in q_{sosed}), the dimensionless spin parameter (a_*), the cosine of the inclination angle for the warm Comptonizing component and the outer disk ($\cos i$), and the redshift (z). As an exploratory study, we consider nonspinning ($a_* = 0$) BHs with a mass range of 10^6 – $10^{10} M_{\odot}$ and accretion rates $-1.5 \leq \log \dot{m} \leq 0$, with 9×7 logarithmically spaced grid points in each direction and intervals of 0.5 and 0.25 dex. We fix the comoving distance $D_c = 1000$ Mpc, redshift $z = 0$, and the inclination at $\cos i = 0.5$ to compute the source SEDs on the M_{BH} – \dot{m} plane.

We focus exclusively on the moderate accretion rate regime of $\log \dot{m} \in [-1.5, 0]$ because of substantial theoretical uncertainties inherent in the slim disk SED model, as well as the imposed lowest accretion rate limit of $-1.65 < \log \dot{m}$ in q_{sosed} . To compare with observables, we do not use the mass accretion rate (\dot{m}) for these theoretical SEDs but instead use the Eddington ratio (λ_{Edd}) based on the bolometric luminosity calculated using the 5100 Å monochromatic luminosity. This detail would lead to λ_{Edd} values at $\log \lambda_{\text{Edd}} < -1.5$ for our theoretical SEDs.

Several example output SEDs from q_{sosed} are displayed in Figure 1. The optical and UV continuum wavelengths used for fiducial luminosity calculations are marked by the gray dashed vertical lines, and the ionizing energy for CIV and hydrogen are shown in blue and red vertical dotted lines, respectively ($h\nu_{\text{CIV}} = 64.5$ eV and $h\nu_{\text{H}} = 13.6$ eV). The upper panel illustrates how the SED varies as the BH mass changes at a fixed accretion rate $\dot{m} = 0.1$. Increasing the mass does not significantly alter the SED shape, but it does increase the overall luminosity and slightly shifts the peak of the multi-temperature blackbody radiation to a lower frequency. The

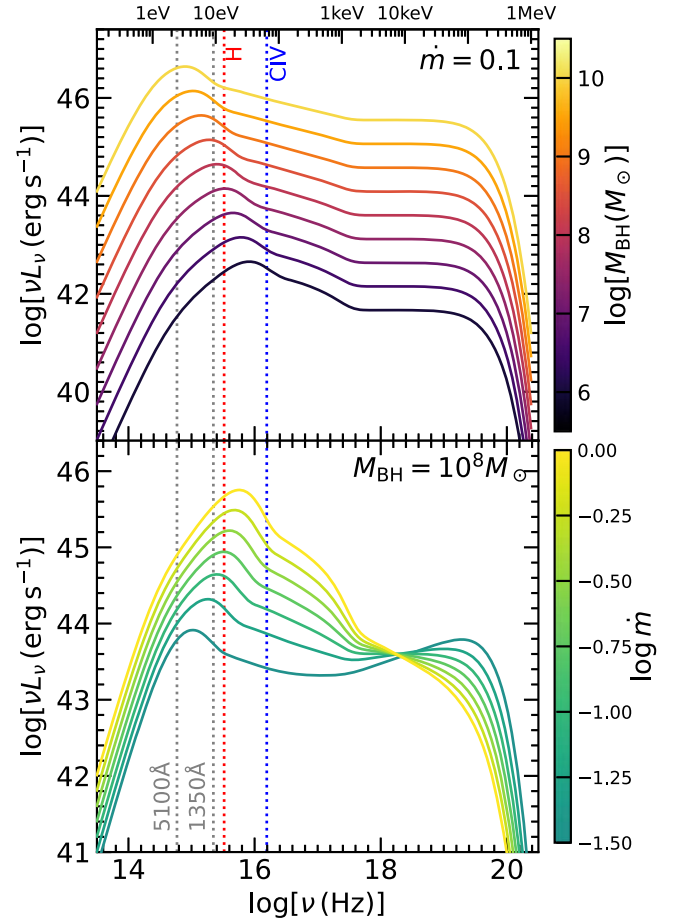


Figure 1. Example of output SEDs generated using XSPEC q_{sosed} . The vertical blue and red dotted lines represent photon energies of $h\nu_{\text{CIV}} = 64.5$ eV and $h\nu_{\text{H}} = 13.6$ eV, respectively. Top panel: SEDs with a constant accretion rate ($\dot{m} = 0.1$) and varying BH mass ($M_{\text{BH}} = 10^6$ – $10^{10} M_{\odot}$) in logarithmic intervals of 0.5 dex. Bottom panel: SEDs with fixed BH mass ($M_{\text{BH}} = 10^8 M_{\odot}$) while varying the accretion rate $\log \dot{m}$ from -1.5 to 0 in logarithmic intervals of 0.25 dex.

lower panel displays the SED variation as a function of accretion rate at a fixed BH mass $M_{\text{BH}} = 10^8 M_{\odot}$. The increasing \dot{m} increases the overall SED of the AGN, pushing the UV peak emission from the thermal disk to higher frequencies and demonstrating a weaker X-ray emission due to changes in the hot flow geometry (A. Kubota & C. Done 2018). Note that the BHs in the lower panel exhibit similar spectral fluxes at around ~ 10 keV, which is due to the hot corona assumption employed in q_{sosed} (see details in Section 4.4). Increasing the BH mass and accretion rate leads to higher optical and UV continuum luminosities (L_{5100} and λL_{1350}), as well as a corresponding increase in the ionizing luminosity, affecting the ratio of line-ionizing fluxes such as CIV/hydrogen.

Figure 2 shows SED comparisons for accretion rates $\dot{m} \in [-1.5, 0]$ at fixed mass (10^6 , 10^7 , 10^8 , 10^9 , and $10^{10} M_{\odot}$). At each BH mass, the SEDs are normalized by the median SED with $\log \dot{m} = -1$. In all panels, higher accretion rates have relatively higher optical and UV luminosities and overall more hydrogen-ionizing flux. Meanwhile, the change in UV luminosity λL_{1350} is more sensitive to accretion rate than λL_{5100} , especially for more massive BHs. To illustrate the significant variations in the SED due to accretion rate changes, Figure 3 presents two theoretical SEDs with similar optical

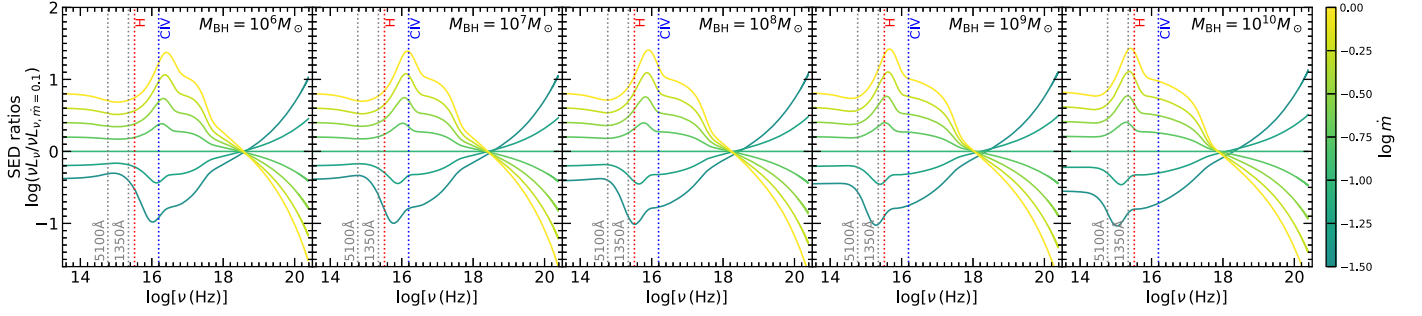


Figure 2. The SED ratios for each BH mass. SEDs are computed for various accretion rates $\log \dot{m} \in [-1.5, 0]$ with 0.25 dex intervals at constant BH mass M_{BH} (from left to right: 10^6 , 10^7 , 10^8 , 10^9 , and $10^{10} M_{\odot}$). Each SED within the panel is normalized relative to the SED with $\dot{m} = 0.1$. Vertical lines are placed at photon energies of $h\nu_{\text{CIV}} = 64.5$ eV (blue) and $h\nu_{\text{H}} = 13.6$ eV (red).

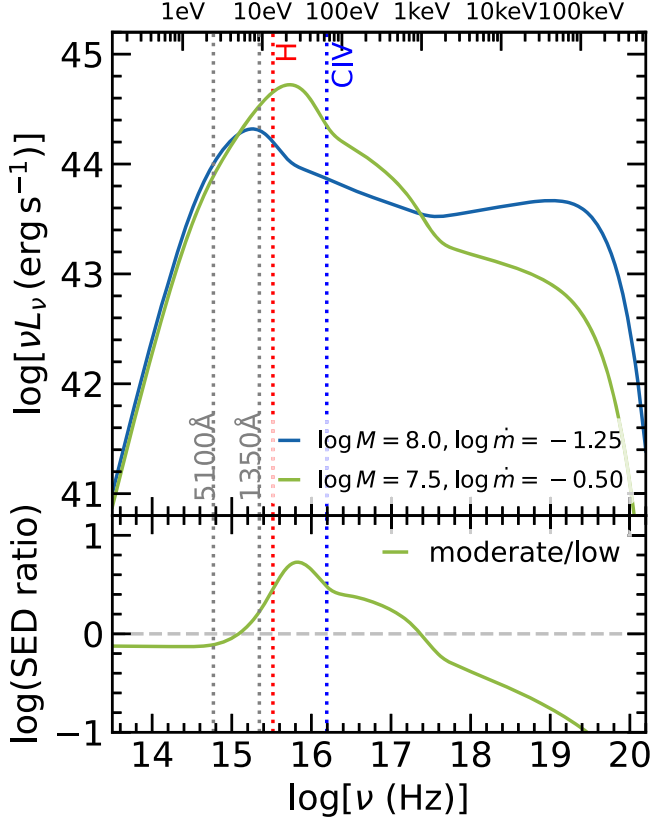


Figure 3. SEDs of two SMBHs with mass M_{BH} of $10^{7.5}$ and $10^8 M_{\odot}$ and accretion rate $\log \dot{m}$ of -0.5 and -1.25 , respectively. These two SEDs with diverse SED shapes produce similar optical luminosities $\log \lambda L_{5100} \sim 44$ but different ionizing fluxes. Within the SSD regime and at fixed optical luminosity, AGNs with higher Eddington ratios (lower BH masses) have relatively more ionizing flux compared with the 5100 \AA flux, which would presumably lead to longer BLR lags.

luminosities $\log \lambda L_{5100} \sim 44$ but different accretion parameters (mass and accretion rate). Given that an increase in \dot{m} and a decrease of M_{BH} shift the UV peak to a higher frequency and soften the SED (Figure 1), the two demonstrated SEDs cross at both optical and soft X-ray wavelengths. Although the optical luminosity is similar, the more massive BH with a lower λ_{Edd} (in blue) produces significantly less hydrogen-ionizing flux and hence is expected to have a shorter $\text{H}\beta$ time lag, if assuming the localization of the BLR is related to the ionizing flux and other properties of the BLR are the same for the two cases.

Figure 4 displays the continuum luminosities computed from q_{SSED} SEDs at three optical/UV wavelengths, with slightly

higher luminosities at shorter wavelengths. While the simulated mass accretion rate ($\log \dot{m}$) ranges from -1.5 to 0 in q_{SSED} , the λ_{Edd} values may fall below -1.5 for the theoretical SEDs due to the universal bolometric correction ($\text{BC} = 9.26$) applied to the continuum luminosity at 5100 \AA . The continuum luminosities show a diagonal increasing trend on the $M_{\text{BH}}-\lambda_{\text{Edd}}$ plane. This trend suggests that despite variations in their underlying SED shapes, BHs with different accretion parameters can produce similar continuum luminosities at fixed observed wavelengths.

This exploratory investigation demonstrates the possible diverse SEDs from AGNs with different accretion parameters. Since the BLR gas clouds are ionized by the ionizing continuum flux, the qualitative changes in the SED shape conceivably can lead to dispersion in the observed $R-L$ relation based on the optical luminosity. We now proceed to use photoionization calculations to make quantitative predictions.

2.2. Photoionization with CLOUDY

We construct detailed photoionization models to calculate line luminosities for individual clouds using CLOUDY (G. J. Ferland et al. 2017; version 17.02) with a spherically symmetric geometry to account for various excitation mechanisms and radiative transfer effects. SEDs computed from Section 2.1 are used as the incident radiation field input. This approach assumes that the BLR gas sees all the radiation from the central source; i.e., there is no inner shielding of the radiation.

Following previous works in a spherically symmetric geometry (K. T. Korista & M. R. Goad 2000, 2004; H. Guo et al. 2020), we assume that the BLR clouds cover a broad range of hydrogen density ($6.0 \leq \log n(\text{H}) [\text{cm}^{-3}] \leq 14.0$) and surface ionization flux ($16.0 \leq \log \Phi(\text{H}) [\text{cm}^{-2}\text{s}^{-1}] \leq 25.0$), both with logarithmic intervals of 0.125 dex. In this section, unless otherwise specified, all physical quantities, such as $n(\text{H})$, $\Phi(\text{H})$, and c , are given in cgs units. The ionization parameter U_{H} is defined as a dimensionless ratio between the hydrogen-ionizing photon flux $Q(\text{H})$ and the total hydrogen density $n(\text{H})$:

$$U_{\text{H}} \equiv \frac{Q(\text{H})}{4\pi R_{\text{BLR}}^2 n(\text{H})c} \equiv \frac{\Phi(\text{H})}{n(\text{H})c}, \quad (2)$$

where R_{BLR} is the distance between the central ionizing source and the illuminated surface of the cloud and c is the speed of light. For each cloud, we assume a hydrogen column density $N_{\text{H}} = 10^{23} \text{ cm}^{-2}$, abundance $Z = Z_{\odot}$, and overall covering factor $CF = 50\%$. Given the full set of hydrogen densities and

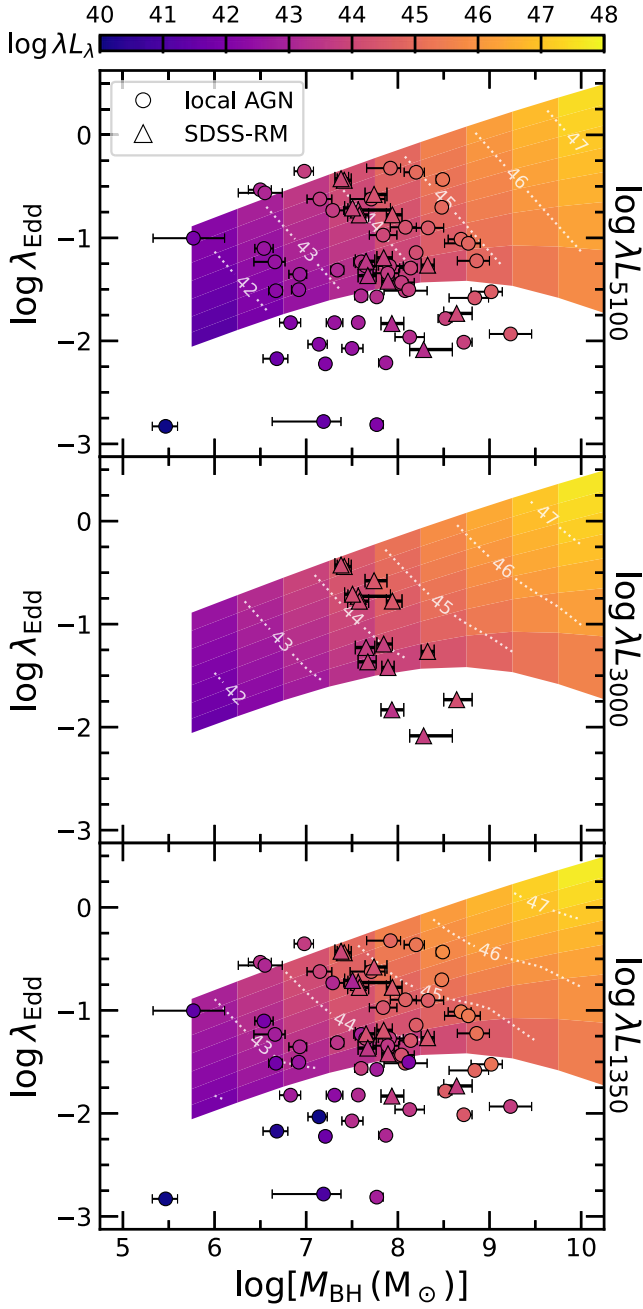


Figure 4. Continuum luminosities at 5100 Å (top), 3000 Å (middle), and 1350 Å (bottom) in the $M_{\text{BH}}-\lambda_{\text{Edd}}$ plane, computed from the q_{SOS} models. Observed continuum luminosities of the compiled RM AGN sample are overlaid in each corresponding panel for comparison. Note that $\lambda_{\text{Edd}} < -1.5$ for certain theoretical SEDs is due to the constant bolometric correction applied to the continuum luminosity at 5100 Å.

ionizing flux, we compute the photoionization results with 4745 calculations for each SED.

The total line luminosity is computed using the LOC model by summing over all grid points with proper weights determined from assumed distribution functions. When summing the grid emissivity, only ionized clouds with a density range of $8.0 \leq \log n(\text{H}) [\text{cm}^{-3}] \leq 12.0$ and ionizing flux $6.0 \leq \log U_{\text{H}} c [\text{cm s}^{-1}] \leq 11.25$ are considered to obtain the radial surface emissivity ($F(r)$; see details in K. T. Korista & M. R. Goad 2000, 2004, 2019; H. Guo et al. 2020). For simplicity, we adopt the empirical assumptions outlined in

J. Baldwin et al. (1995): $f(r) \propto r^{\Gamma}$ and $g(n) \propto n^{\beta}$ ($\beta = -1$) for the cloud distribution, which represent the cloud coverage fractions as functions of radius and gas density, respectively. This assumption ensures equal weighting for each grid point in the density–flux plane on a logarithmic scale. In previous studies, K. T. Korista & M. R. Goad (2000, 2019) proposed $-1.4 < \Gamma < -1$ and fixed $\Gamma = -1.2$ for NGC 5548, and H. Guo et al. (2020) employed $\Gamma = -1.1$ to align with the observed Mg II luminosity; therefore, after comparing with observed line luminosities in Section 3.2, we fix $\Gamma = -1.1$ to match the observed lines. The observed line luminosity is

$$L_{\text{line}} \propto \int \int_{R_{\text{in}}}^{R_{\text{out}}} r^2 F(r) f(r) g(n) dn dr, \\ \propto \int d(\log n) \int_{R_{\text{in}}}^{R_{\text{out}}} r^{1.9} F(r) d(\log r), \quad (3)$$

where $F(r)$ is the radial surface emissivity of a single cloud. The BLR sizes predicted in Section 2.3 are adopted as the average distance for the integral.

2.3. Predictions of BLR Size

The relation between BLR radius $R_{\text{BLR}} = c\tau$ and monochromatic luminosity can be calculated using this grid of SEDs. We use the following expression to compute the average distance between the ionizing source center and the Balmer-line-emitting clouds:

$$R_{\text{BLR}} = \sqrt{\frac{Q(\text{H})}{4\pi\Phi(\text{H})}} = \sqrt{\frac{\int_{\nu}^{\infty} \frac{\pi L_{\nu}}{h\nu} d\nu}{4\pi\Phi(\text{H})}}, \quad (4)$$

where $\Phi(\text{H}) = U_{\text{H}} n(\text{H}) c$ is the flux of ionizing photons received by the clouds. The LOC model assumes that the clouds with the highest reprocessing efficiency dominate the observed emissions. Hydrogen and helium emission lines, in particular, exhibit peak reprocessing efficiency under conditions of low ionizing photon flux and high hydrogen density ($\log n(\text{H}) [\text{cm}^{-3}] \gtrsim 12$; e.g., J. Baldwin et al. 1995; K. Korista et al. 1997; K. T. Korista & M. R. Goad 2000). Moreover, comparisons of several AGN emission line ratios with the photoionization of the dominant cloud have consistently indicated a product of the ionization parameter and hydrogen density approximating $\log U_{\text{H}} n(\text{H}) [\text{cm}^{-3}] \sim 10$ (with $\log n(\text{H}) [\text{cm}^{-3}] \sim 9.6\text{--}12.6$ and $\log U_{\text{H}} \sim -2.8$ to -2.0 ; e.g., T. A. A. Sigut & A. K. Pradhan 2003; Y. Matsuoka et al. 2008; C. A. Negrete et al. 2012). Therefore, a constant ionization parameter $\log U_{\text{H}} = -2.0$ and hydrogen density $n(\text{H}) = 10^{12} \text{cm}^{-3}$ are adopted here to calculate the BLR gas distance (Equation (4)).

Figure 5 compares our predicted H β BLR time lag as a function of the monochromatic luminosity at 5100 Å with our compiled RM AGN sample (see details in Section 3). We divide the observed RM sample into narrow mass bins with $\Delta \log M_{\text{BH}} = 0.5$ and assign them to their respective mass bins in Figure 5. Within each subplot, the predicted time lags are depicted by colored bands, and all data points are color-coded based on their Eddington ratio. As shown in Figure 5, our predicted time lag trends with optical luminosity are in overall agreement with the observed lags given the assumed universal values of the ionization parameter and cloud hydrogen density. This consistency supports the general notion that the BLR

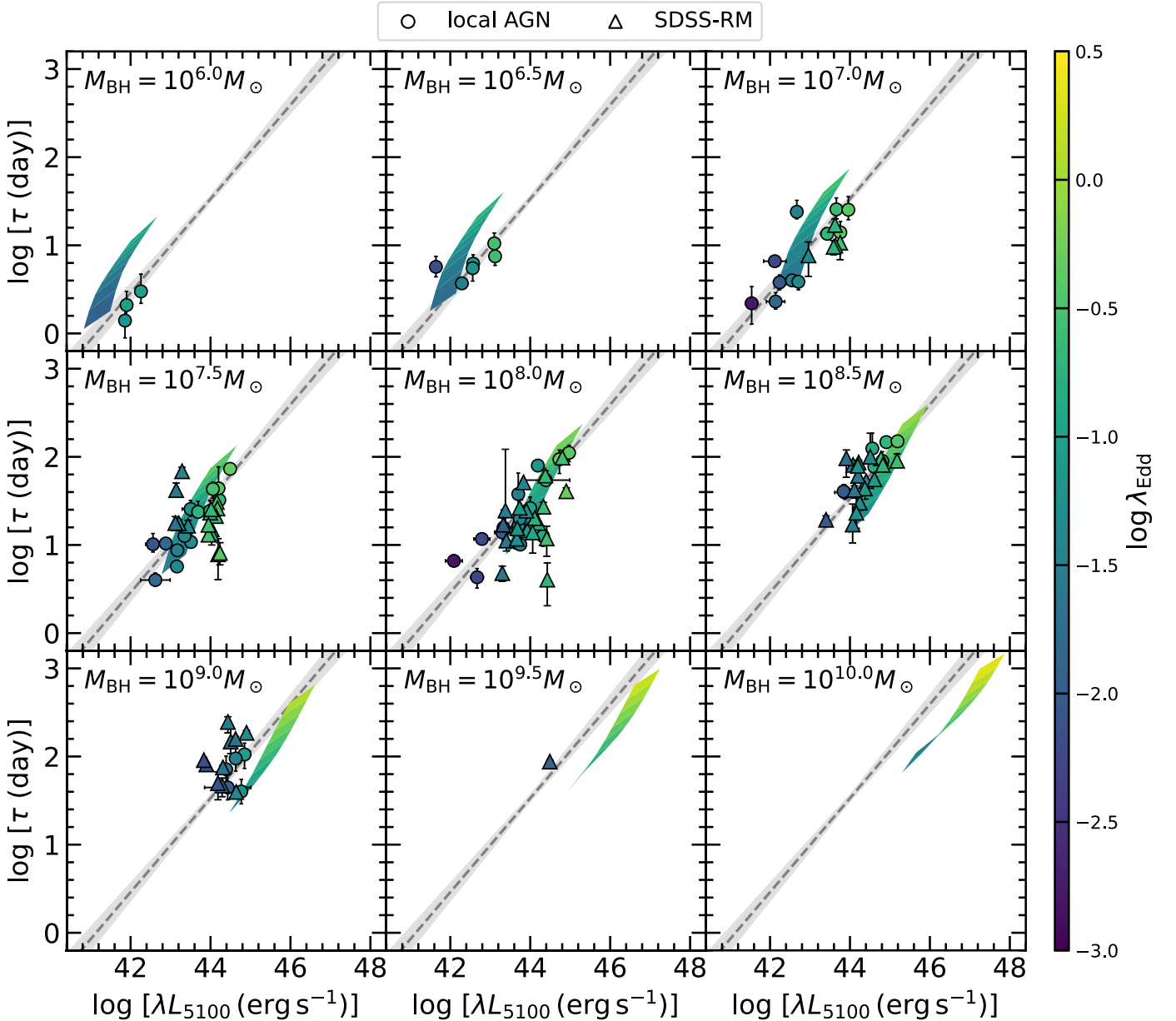


Figure 5. Dependence of the H β BLR time lag on monochromatic luminosity at 5100 \AA across a range of mass bins (from $\log M_{\text{BH}} = 6$ to $\log M_{\text{BH}} = 10$ with $\Delta \log M_{\text{BH}} = 0.5$). Predicted time lags are represented by shaded bands with varying colors denoting different Eddington ratios. Observed H β time lags are presented as circles and triangles for low-accretion ($\lambda_{\text{Edd}} < 0.5$) local AGNs and SDSS-RM sources, respectively, with the same color scheme as the theoretical predictions. The gray dashed line indicates the canonical R - L relation from M. C. Bentz et al. (2013), with a slope $\alpha = 0.533^{+0.533}_{-0.033}$ and an intercept $\beta = 1.527 \pm 0.031$ at $\log \lambda(L_{5100}/\text{erg s}^{-1}) = 44$.

responds to the ionizing continuum. While the assumed photoionization parameters could reproduce the overall trend in the R - L plane across a range of BH mass, discrepancies in measured accretion parameters and/or assumptions in our theoretical calculations for individual objects may lead to deviations from the predicted time lags; these observational and theoretical uncertainties are discussed in Section 4.

3. Comparison with Observations

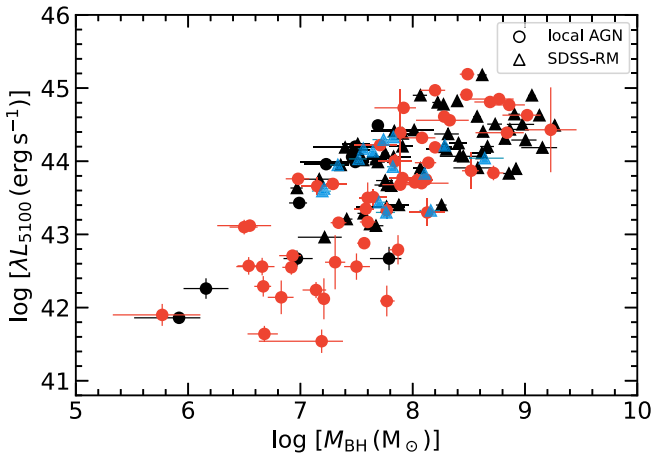
3.1. Sample and Data

We start from the sample of ~ 140 $z \lesssim 0.5$ broad-line AGNs with H β RM measurements and select those with $10^{-3} < \lambda_{\text{Edd}} < 0.5$ in the SSD regime as our primary sample.

Figure 6 shows the distribution of BH mass M_{BH} measured from H β RM versus their optical luminosity λL_{5100} for this primary sample, including objects with and without UV spectroscopy. For M_{BH} values of these local RM AGNs, we combine the catalog in M. C. Bentz & S. Katz (2015) and Table 1 in P. Du & J.-M. Wang (2019) and correct M_{BH} using a nominal virial factor $f_{\text{FWHM,H}\beta} = 1.12$ from J.-H. Woo et al. (2015). The host contamination in λL_{5100} has been subtracted for the local AGNs, except for eight sources (Zw 229+015, Mrk 1501, H0507+164, Mrk 704, PG 0934+013, Mrk 50, NGC 4395, and Mrk 6), for which we adopt their average λL_{5100} from light curves as an upper limit. We supplement the local RM AGNs with 72 more distant quasars from the SDSS-RM sample (Y. Shen et al. 2024). The host contamination for

Table 1
Target Properties

RMID	R.A. (J2000) (deg)	Decl. (J2000) (deg)	z	$\tau_{H\beta}$ (days)	$\log(M_{\text{BH, RM}})$ (M_{\odot})	NUV (mag)
RM101	213.059	53.430	0.458	$21.4^{+4.2}_{-6.4}$	$7.26^{+0.09}_{-0.12}$	19.35
RM160	212.672	53.314	0.360	$21.9^{+4.2}_{-2.4}$	$7.85^{+0.09}_{-0.07}$	20.77
RM177	214.352	52.507	0.482	$10.1^{+12.5}_{-2.7}$	$7.57^{+0.35}_{-0.11}$	20.80
RM229	212.575	53.494	0.470	$16.2^{+2.9}_{-4.5}$	$7.65^{+0.09}_{-0.12}$	20.77
RM267	212.803	53.752	0.588	$20.4^{+2.5}_{-2.0}$	$7.41^{+0.08}_{-0.08}$	20.16
RM272	214.107	53.911	0.263	$15.1^{+3.2}_{-4.6}$	$7.58^{+0.10}_{-0.13}$	19.40
RM301	215.043	52.675	0.548	$12.8^{+5.7}_{-4.5}$	$8.64^{+0.17}_{-0.14}$	21.10
RM305	212.518	52.528	0.527	$53.5^{+4.2}_{-4.0}$	$8.32^{+0.07}_{-0.07}$	20.28
RM320	215.161	53.405	0.265	$25.2^{+4.7}_{-5.7}$	$7.67^{+0.09}_{-0.11}$	20.60
RM371	212.848	52.225	0.473	$13.0^{+1.4}_{-0.8}$	$7.38^{+0.08}_{-0.07}$	20.21
RM622	212.813	51.869	0.572	$49.1^{+11.1}_{-2.0}$	$7.94^{+0.11}_{-0.06}$	20.55
RM694	214.278	51.728	0.532	$10.4^{+6.3}_{-3.0}$	$6.70^{+0.20}_{-0.15}$	20.83
RM720	211.325	53.258	0.467	$41.6^{+14.8}_{-8.3}$	$7.74^{+0.14}_{-0.10}$	19.80
RM772	215.400	52.527	0.249	$3.9^{+0.9}_{-0.9}$	$6.60^{+0.10}_{-0.10}$	19.92
RM781	215.265	51.972	0.264	$75.2^{+3.2}_{-3.3}$	$7.89^{+0.07}_{-0.07}$	20.47
RM782	213.329	54.534	0.363	$20.0^{+1.1}_{-3.0}$	$7.51^{+0.06}_{-0.09}$	19.50
RM790	214.372	53.307	0.238	$5.5^{+3.7}_{-2.1}$	$8.28^{+0.31}_{-0.15}$	20.10
RM840	214.188	54.428	0.244	$5.0^{+1.5}_{-1.4}$	$7.93^{+0.13}_{-0.12}$	19.94

Note. Properties of the 18 quasars proposed in HST GO-16171. RM BH masses are based on $H\beta$ lags from C. J. Grier et al. (2017). Time lags are rest-frame values.**Figure 6.** BH mass measurements from $H\beta$ RM and optical luminosity λL_{5100} for local AGNs at $z < 0.5$ are represented by circles (P. Du & J.-M. Wang 2019), while the SDSS-RM sample is coded by triangles (C. J. Grier et al. 2017; Y. Shen et al. 2019, 2024). Objects lacking ultraviolet spectra are indicated in black, whereas those with ultraviolet spectra are distinguished by colors, with local AGNs in red and the SDSS-RM sample in blue.

the SDSS-RM quasars used in this work is removed based on a spectral decomposition approach described in Y. Shen et al. (2015b). We use a bolometric correction of $BC = 9.26$ (G. T. Richards et al. 2006) for the optical continuum at 5100 Å to calculate the bolometric luminosity L_{bol} and the RM mass M_{BH} for the dimensionless Eddington ratio.

After assembling the primary sample of 135 low-to-moderate-accretion AGNs with $H\beta$ RM measurements, we select a subsample of quasars with both rest-frame UV and optical spectra. We acquired UV spectroscopy for 18 SDSS-RM quasars at $0.2 \lesssim z \lesssim 0.6$ from a dedicated Hubble Space Telescope (HST) Space Telescope Imaging Spectrograph (STIS) program in Cycle 28 (GO-16171; PI: Shen). These quasars are selected from the SDSS-RM sample

(Y. Shen et al. 2015a) with direct RM lags and BH masses based on the broad $H\beta$ line (C. J. Grier et al. 2017). We restrict to quasars with $0.2 \lesssim z \lesssim 0.6$ and Galaxy Evolution Explorer (GALEX) near-ultraviolet (NUV) $\lesssim 21$ mag while spanning a broad range in luminosity and $H\beta$ lags to sample the parameter space. Table 1 summarizes the properties of the 18 SDSS-RM targets.

The 18 SDSS-RM quasars were observed with HST/STIS in spectroscopic mode with the NUV-MAMA G230L grating to optimize the spectral coverage. This instrumental configuration provides broad spectral coverage from 1570 to 3180 Å, which covers the dominant UV emission lines from Si IV to C III] for our targets. The brightnesses of our targets vary with GALEX NUV ~ 19 –21: for the brightest 12 targets, one full orbit exposure time is utilized, five quasars (RM160, RM177, RM229, RM320, and RM694) were observed for two orbits, and the faintest target with a GALEX NUV magnitude of 21.1 (RM301) was observed with three orbits. The initial visits of all targets lasted from 2020 December to 2022 February; however, four targets (RM177, RM229, RM320, and RM694) suffered from the failure of guide-star acquisition at the start of the second orbit, resulting in lost data. Repeat visits for those targets were approved and recurred from 2022 September to November. The pipeline-processed STIS spectra of those targets with multiple orbits of exposure were coadded to improve the signal-to-noise ratio (S/N) of our sample. The observed spectra are presented in Figure 7.

For the remaining local RM AGNs in our sample, in addition to our SDSS-RM quasars, we collect archival UV spectroscopy from the International Ultraviolet Explorer, the STIS, and the Cosmic Origins Spectrograph on HST. If multiple spectra exist in the public archives for a given object, either multiple epochs taken with the same instrument or from multiple instruments, we combined the spectra for each object via the standard weighted average method. Since the disk structure of high-accretion SMBHs will have a dramatic impact on the ionizing continuum illuminating the BLR, we only focus on the low-to-moderate-accretion sample in this work.

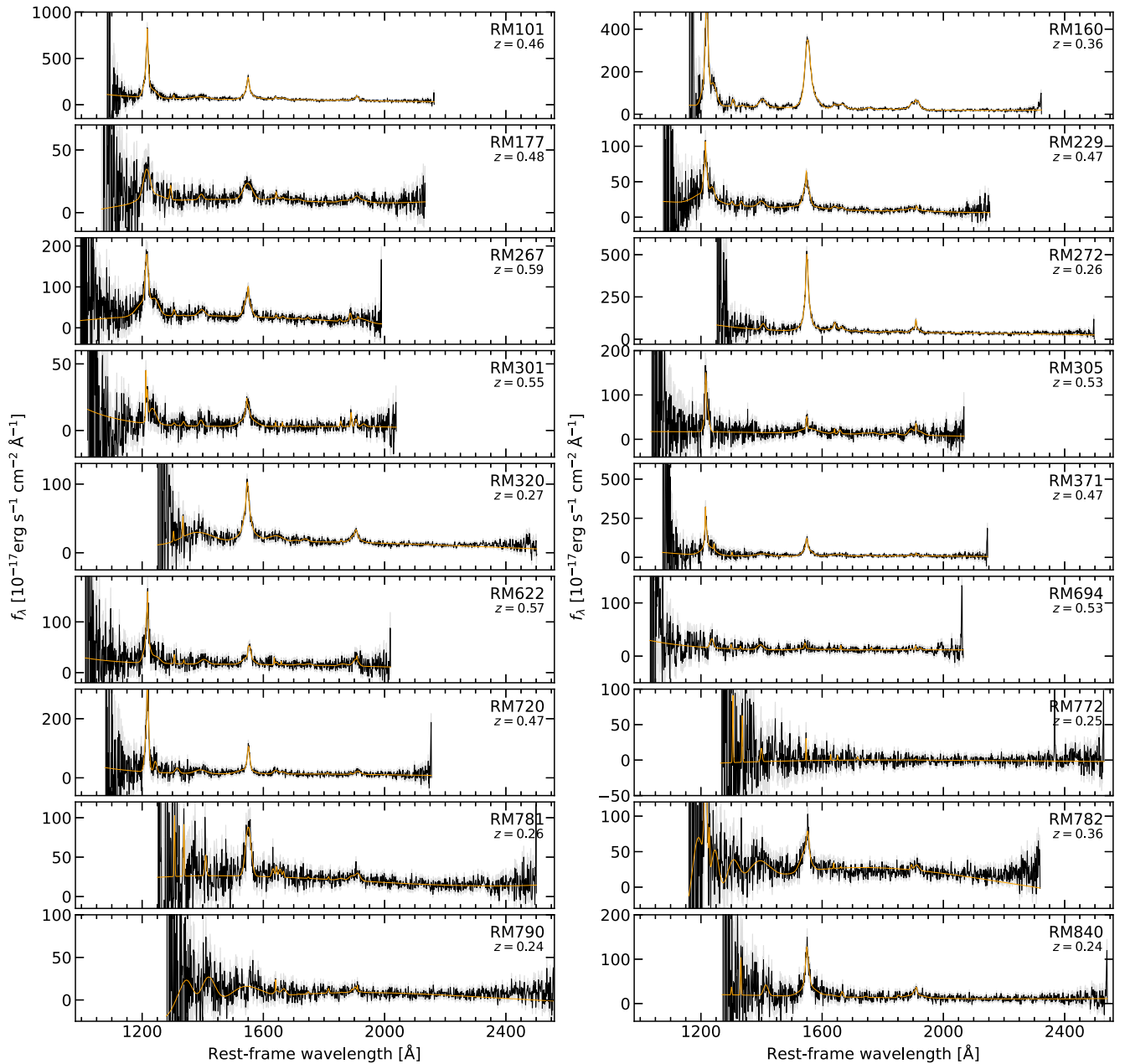


Figure 7. UV spectra of the 18 quasars observed by HST/STIS under the program HST GO-16171. The data have been corrected for the galactic reddening and shifted to the rest frame. The orange lines demonstrate our fitting results.

Our final sample includes 15 SDSS-RM quasars and 52 local RM AGNs with accretion rates $10^{-3} < \lambda_{\text{Edd}} < 0.5$. We then apply the spectral decomposition code PyQSOFit (H. Guo et al. 2018) with minor custom adjustments to measure their UV spectral properties and summarize them in Table 2. The optical spectral properties ($\log \lambda L_{5100}$, $H\beta$, and $\text{He II } \lambda 4687$) for the SDSS-RM sample are from Y. Shen et al. (2019), while those of local AGNs are from P. Du & J.-M. Wang (2019).

3.2. UV/Optical Line Strengths

Figure 8 presents the comparison of ionizing luminosities, LOC-predicted line luminosities, and observed line luminosities for various emission lines in the $M_{\text{BH}}-\lambda_{\text{Edd}}$ plane. In the left panel, we compute the ionizing luminosities using the integral expression $L_{\text{ion}} = \int_{\nu_{\text{product}}}^{\nu_{\text{destruct}}} L_{\nu} d\nu$ with the production

and destruction edges: 47.9 and 64.5 eV for C IV, 7.6 and 15.0 eV for Mg II, 24.6 and 54.4 eV for He II $\lambda 1640$, and 13.6 eV for $H\beta$. The middle panels display the line luminosities predicted by the LOC model using Equation (3) (see Section 2.2). The right panels present the observed line luminosities for both local RM AGNs and the SDSS-RM sample. For local RM AGNs, $H\beta$ line luminosities are from P. Du & J.-M. Wang (2019). The line luminosities for $H\alpha$, $H\beta$, and He II $\lambda 4687$ in the SDSS-RM sample are from Y. Shen et al. (2019). There are offsets of ~ 1 dex in the observed C III], He II $\lambda 4687$, and He II $\lambda 1640$ emission line luminosities to the LOC prediction, which may be a result of the underestimated EUV SED and the simplified assumptions of the BLR cloud distribution. Despite these offsets, all panels in Figure 8 exhibit a positive correlation in the $M_{\text{BH}}-\lambda_{\text{Edd}}$ plane. Most importantly, this coherent trend between the LOC predictions and

Table 2
RM AGN UV+Optical Spectroscopic Properties

Objects	$\log \lambda L_{5100}$ (erg s^{-1})	$\log \lambda L_{1350}$ (erg s^{-1})	$\log L_{\text{CIV}}$ (erg s^{-1})	REW (C IV) (\AA)	C IV Blueshift (km s^{-1})	$\log L_{\text{CIII}}$ (erg s^{-1})	REW (C III) (\AA)	$\log L_{\text{HeII}1640}$ (erg s^{-1})	REW (He II 1640) (\AA)	$\log L_{\text{MgII}}$ (erg s^{-1})	REW (Mg II) (\AA)	$\log L_{\text{H}\beta}$ (erg s^{-1})	REW (H β) (\AA)	$\log L_{\text{HeII}4687}$	REW (He II 4687)
RM160	43.79 ± 0.01	44.34 ± 0.02	43.62 ± 0.01	321.2 ± 5.7	-595 ± 45	42.47 ± 0.03	33.0 ± 2.5	42.19 ± 0.09	13.0 ± 2.7	42.07 ± 0.01	96.5 ± 1.4	40.9 ± 0.06	6.4 ± 0.6
RM177	43.97 ± 0.01	44.08 ± 0.03	42.64 ± 0.03	47.7 ± 3.9	145 ± 366	42.32 ± 0.09	29.5 ± 5.7	41.37 ± 0.23	2.7 ± 2.5	42.31 ± 0.01	62.0 ± 1.7	41.4 ± 0.02	7.5 ± 0.4
RM229	43.56 ± 0.01	44.25 ± 0.03	43.0 ± 0.05	100.1 ± 9.1	198 ± 504	42.35 ± 0.27	36.4 ± 16.5	41.83 ± 0.24	7.8 ± 6.5	41.93 ± 0.02	62.0 ± 2.3	40.86 ± 0.15	5.2 ± 2.5
RM267	44.11 ± 0.01	44.76 ± 0.02	43.26 ± 0.02	46.7 ± 2.1	332 ± 166	42.94 ± 0.12	47.6 ± 14.0	42.54 ± 0.02	81.1 ± 4.2	41.33 ± 0.17	4.8 ± 2.5
RM272	43.94 ± 0.01	44.26 ± 0.05	43.16 ± 0.04	145.4 ± 15.3	-287 ± 127	42.24 ± 0.05	21.0 ± 2.6	42.2 ± 0.32	17.1 ± 9.5	42.37 ± 0.01	132.2 ± 0.6	41.46 ± 0.01	15.8 ± 0.5
RM301	44.04 ± 0.01	43.75 ± 0.09	42.82 ± 0.03	183.9 ± 12.4	304 ± 193	41.83 ± 0.23	20.4 ± 11.7	42.27 ± 0.01	58.7 ± 1.2	40.75 ± 0.08	1.7 ± 0.3
RM305	44.19 ± 0.01	44.37 ± 0.04	42.91 ± 0.04	54.5 ± 5.2	-1210 ± 881	42.61 ± 0.18	40.5 ± 17.8	41.47 ± 0.33	2.1 ± 2.4	42.53 ± 0.04	77.7 ± 6.2	41.4 ± 0.02	5.6 ± 0.3
RM320	43.44 ± 0.01	43.59 ± 0.06	42.68 ± 0.04	138.7 ± 13.4	407 ± 266	41.92 ± 0.05	25.5 ± 2.9	42.02 ± 0.26	29.9 ± 13.2	41.89 ± 0.01	74.9 ± 1.9	41.18 ± 0.12	14.2 ± 4.7
RM371	44.09 ± 0.01	44.03 ± 0.1	43.17 ± 0.04	205.4 ± 24.3	1165 ± 435	42.42 ± 0.28	37.0 ± 13.8	42.27 ± 0.11	25.4 ± 6.3	42.4 ± 0.01	101.6 ± 2.0	40.66 ± 0.14	1.8 ± 0.6
RM622	44.3 ± 0.01	44.49 ± 0.03	43.03 ± 0.07	49.8 ± 7.5	-1222 ± 609	42.54 ± 0.24	20.8 ± 9.9	41.85 ± 0.26	3.5 ± 3.4	42.62 ± 0.01	81.1 ± 1.1	41.14 ± 0.04	2.6 ± 0.3
RM720	44.3 ± 0.01	44.22 ± 0.04	43.1 ± 0.07	114.3 ± 16.7	-328 ± 240	42.29 ± 0.14	20.4 ± 5.2	42.29 ± 0.09	18.0 ± 3.8	42.46 ± 0.01	61.8 ± 0.4	41.5 ± 0.03	6.4 ± 0.5
RM781	43.6 ± 0.01	43.88 ± 0.09	42.49 ± 0.05	55.1 ± 5.9	-189 ± 343	41.63 ± 0.15	10.0 ± 4.0	41.36 ± 0.24	4.2 ± 4.1	41.91 ± 0.02	65.8 ± 2.8	41.27 ± 0.05	14.6 ± 1.6
RM782	43.93 ± 0.01	43.04 ± 0.31	42.82 ± 0.04	66.3 ± 5.9	-586 ± 431	41.8 ± 0.11	6.0 ± 1.5	42.0 ± 0.01	37.0 ± 0.5	40.5 ± 0.06	1.1 ± 0.2
RM790	43.33 ± 0.01	41.29 ± 0.18	13.4 ± 4.7	41.16 ± 0.3	20.2 ± 15.1	41.87 ± 0.03	53.9 ± 3.2	24.03 ± 8.55	0.0 ± 5.0
RM840	43.24 ± 0.01	43.66 ± 0.13	42.65 ± 0.05	153.7 ± 17.4	-218 ± 269	42.07 ± 0.07	53.3 ± 7.3	41.47 ± 0.31	10.8 ± 5.2	41.6 ± 0.01	38.9 ± 0.7	39.47 ± 19.82	0.3 ± 0.2
Mrk 335	43.76 ± 0.07	43.72 ± 0.01	42.63 ± 0.01	108.2 ± 1.8	-127 ± 23	42.8 ± 0.02	135.6 ± 7.5	41.5 ± 0.02	7.9 ± 0.3	41.91 ± 0.03	15.5 ± 1.0	42.09 ± 0.09	108.2 ± 0.1
PG 0026	44.97 ± 0.02	45.26 ± 0.01	43.55 ± 0.01	32.8 ± 1.1	-993 ± 129	42.8 ± 0.15	6.5 ± 3.7	42.93 ± 0.04	46.2 ± 0.0
PG 0052	44.81 ± 0.03	45.36 ± 0.01	44.18 ± 0.03	113.7 ± 7.6	670 ± 51	42.53 ± 0.18	3.8 ± 2.4	42.47 ± 0.61	2.5 ± 9.0	43.13 ± 0.05	107.4 ± 0.0
Fairall 9	43.98 ± 0.04	44.43 ± 0.01	43.33 ± 0.01	114.9 ± 0.9	61 ± 24	42.68 ± 0.12	29.0 ± 10.2	42.53 ± 0.18	19.1 ± 5.4	42.84 ± 0.01	53.5 ± 0.5	42.67 ± 0.04	249.8 ± 0.0
Mrk 590	43.5 ± 0.21	42.92 ± 0.01	42.27 ± 0.01	710.5 ± 7.3	356 ± 89	40.18 ± 0.3	2.4 ± 9.4	40.92 ± 0.09	32.4 ± 7.0	41.92 ± 0.01	48.1 ± 0.8	41.85 ± 0.12	108.6 ± 0.1
Mrk 1044	43.1 ± 0.1	43.42 ± 0.01	41.85 ± 0.01	42.7 ± 0.3	865 ± 26	41.08 ± 0.21	10.0 ± 7.1	41.58 ± 0.01	24.8 ± 0.7	40.93 ± 0.06	10.9 ± 1.5	41.39 ± 0.09	101.4 ± 0.1
3C 120	44.0 ± 0.1	44.41 ± 0.01	43.31 ± 0.01	134.9 ± 1.5	13 ± 38	42.04 ± 0.1	10.5 ± 2.4	42.39 ± 0.02	17.7 ± 0.8	42.67 ± 0.01	72.3 ± 1.3	42.36 ± 0.04	118.8 ± 0.0
Ark 120	43.87 ± 0.25	44.61 ± 0.01	43.32 ± 0.01	77.9 ± 1.0	20 ± 25	42.91 ± 0.04	36.2 ± 3.3	42.69 ± 0.12	18.8 ± 4.1	42.76 ± 0.01	37.5 ± 0.4	42.54 ± 0.13	244.8 ± 0.1
MCG 811	43.33 ± 0.11	42.81 ± 0.04	41.91 ± 0.01	172.7 ± 5.5	643 ± 170	41.54 ± 0.16	45.5 ± 13.7	41.15 ± 0.04	27.2 ± 2.8	41.96 ± 0.01	72.3 ± 1.1	41.66 ± 0.09	108.7 ± 0.1
Mrk 374	43.77 ± 0.04	43.72 ± 0.02	42.8 ± 0.06	206.6 ± 26.5	-20 ± 227	41.76 ± 0.11	24.9 ± 7.5	40.56 ± 0.63	1.3 ± 9.5	41.91 ± 0.04	43.1 ± 3.5	41.83 ± 0.04	58.3 ± 0.0
Mrk 79	43.68 ± 0.07	43.59 ± 0.01	42.46 ± 0.01	115.7 ± 3.7	2446 ± 75	42.0 ± 0.05	46.9 ± 4.7	42.06 ± 0.05	49.0 ± 4.5	41.75 ± 0.02	26.2 ± 1.5	41.9 ± 0.05	85.4 ± 0.0
Mrk 382	43.12 ± 0.08	43.15 ± 0.01	40.15 ± 0.18	16.4 ± 7.1	41.01 ± 0.05	39.6 ± 0.0
PG 0804	44.91 ± 0.02	45.36 ± 0.01	44.04 ± 0.01	87.5 ± 1.4	-923 ± 596	42.66 ± 0.19	6.3 ± 4.1	42.78 ± 0.06	5.3 ± 0.7	43.0 ± 0.04	19.2 ± 1.7	43.29 ± 0.03	122.5 ± 0.0
PG 0844	44.22 ± 0.07	44.59 ± 0.01	43.01 ± 0.02	38.6 ± 1.5	-141 ± 59	42.8 ± 0.18	28.3 ± 8.9	42.67 ± 0.02	18.6 ± 1.0	42.27 ± 0.08	11.3 ± 2.4	42.56 ± 0.05	111.2 ± 0.0
Mrk 110	43.66 ± 0.12	43.92 ± 0.01	43.05 ± 0.01	186.4 ± 2.1	-762 ± 37	41.92 ± 0.08	14.5 ± 2.7	42.02 ± 0.01	17.3 ± 0.6	42.4 ± 0.01	65.2 ± 0.5	42.03 ± 0.08	123.8 ± 0.1
PG 0953	45.19 ± 0.01	45.79 ± 0.01	44.71 ± 0.02	334.5 ± 17.5	52 ± 52	43.29 ± 0.04	64.7 ± 0.0
NGC 3227	42.24 ± 0.11	39.99 ± 0.12	39.74 ± 0.1	50.8 ± 9.4	38.66 ± 0.15	18.5 ± 9.3	40.17 ± 0.01	38.7 ± 1.0	40.38 ± 0.1	71.0 ± 0.1
NGC 3516	42.79 ± 0.2	43.11 ± 0.01	41.8 ± 0.01	69.3 ± 0.4	-1711 ± 73	41.74 ± 0.12	71.4 ± 14.8	41.04 ± 0.01	12.3 ± 0.3	41.5 ± 0.02	77.4 ± 2.8	41.06 ± 0.18	94.0 ± 0.2
SBS 1116	42.14 ± 0.23	42.85 ± 0.01	41.95 ± 0.02	231.6 ± 13.5	-220 ± 62	41.12 ± 0.04	39.8 ± 3.8	40.72 ± 0.07	14.7 ± 2.6	41.02 ± 0.04	38.2 ± 3.4	40.7 ± 0.07	186.8 ± 0.1
Arp 151	42.55 ± 0.1	42.6 ± 0.01	41.76 ± 0.02	233.0 ± 8.6	-2167 ± 132	41.02 ± 0.05	52.1 ± 5.5	40.39 ± 0.06	10.6 ± 1.5	40.89 ± 0.01	47.3 ± 0.8	40.95 ± 0.11	130.0 ± 0.1
NGC 3783	42.56 ± 0.18	43.34 ± 0.01	42.4 ± 0.01	171.1 ± 2.5	-137 ± 29	41.7 ± 0.1	32.7 ± 7.1	41.29 ± 0.02	13.4 ± 0.6	41.83 ± 0.01	54.9 ± 1.2	41.01 ± 0.18	144.0 ± 0.2
Mrk 1310	42.29 ± 0.14	41.76 ± 0.01	41.23 ± 0.03	485.7 ± 37.6	-183 ± 250	40.1 ± 0.27	28.7 ± 31.6	40.65 ± 0.06	64.7 ± 9.4	40.56 ± 0.1	94.3 ± 0.1
NGC 4051	41.9 ± 0.15	41.36 ± 0.01	39.99 ± 0.01	62.1 ± 1.4	482 ± 516	39.79 ± 0.1	35.7 ± 7.5	39.35 ± 0.02	13.9 ± 0.7	40.03 ± 0.01	61.1 ± 1.8	40.09 ± 0.19	78.6 ± 0.2
NGC 4151	42.09 ± 0.21	42.9 ± 0.02	42.12 ± 0.01	210.0 ± 2.6	139 ± 44	41.36 ± 0.03	37.3 ± 2.4	40.76 ± 0.02	8.9 ± 0.4	41.37 ± 0.01	46.3 ± 0.7	40.56 ± 0.2	150.8 ± 0.2
PG 1211	44.73 ± 0.08	44.9 ± 0.01	43.74 ± 0.02	111.8 ± 5.5	499 ± 28	43.04 ± 0.07	28.8 ± 4.5	42.55 ± 0.04	7.6 ± 0.7	42.38 ± 0.06	7.3 ± 1.0	43.02 ± 0.06	100.2 ± 0.1
NGC 4253	42.57 ± 0.12	41.9 ± 0.03	40.48 ± 0.06	61.6 ± 7.9	35 ± 267	39.6 ± 0.25	8.2 ± 11.3	40.41 ± 0.08	30.7 ± 5.8	40.77 ± 0.12	81.1 ± 0.1
PG 1229	43.7 ± 0.05	44.56 ± 0.01	43.19 ± 0.01	62.3 ± 2.0	1038 ± 183	42.78 ± 0.04	29.8 ± 2.3	42.74 ± 0.12	22.9 ± 4.9	42.52 ± 0.02	27.7 ± 1.5	42.31 ± 0.06	209.7 ± 0.1
NGC 4593	42.62 ± 0.37	42.36 ± 0.01	41.5 ± 0.01	198.8 ± 1.2	-113 ± 32	40.66 ± 0.21	21.6 ± 11.8	40.42 ± 0.24	15.4 ± 14.0	41.14 ± 0.01	61.7 ± 0.6	40.95 ± 0.33	108.3 ± 0.3
NGC 4748	42.56 ± 0.12	42.87 ± 0.01	41.52 ± 0.02	70.4 ± 3.5	-1069 ± 559	41.66 ± 0.07	110.9 ± 15.9	41.22 ± 0.08	36.5 ± 6.6	40.99 ± 0.01	31.3 ± 0.9	40.98 ± 0.1	136.8 ± 0.1
PG 1307	44.85 ± 0.02	45.34 ± 0.01	44.06 ± 0.02	90.0 ± 3.9	975 ± 56	42.6 ± 0.12	6.8 ± 1.8	43.13 ± 0.06	98.4 ± 0.1
MCG 630	41.64 ± 0.11	40.25 ± 0.37	39.92 ± 0.21	80.6 ± 45.2	39.85 ± 0.19	91.0 ± 0.2
NGC 5273	41.54 ± 0.16	41.0 ± 0.05	39.89 ± 0.1	175.2 ± 37.2	-352 ± 736	39.62 ± 0.29	277.1 ± 131.1	39.29 ± 0.27	54.9 ± 22.4	38.54 ± 0.16	9.6 ± 3.6	39.74 ± 0.11	82.2 ± 0.1
Mrk 279	43.71 ± 0.07	43.99 ± 0.01	41.76 ± 0.02	9.7 ± 0.5	1160 ± 184	41.79 ± 0.23	13.7 ± 12.7	41.53 ± 0.02	6.1 ± 0.3	42.12 ± 0.06	132.2 ± 0.1
PG 1411	44.56 ± 0.02	44.65 ± 0.01	43.33 ± 0.02	72.1 ± 2.4	-1619 ± 77	43.15 ± 0.35	57.8 ± 33.8	42.31 ± 0.03	7.2 ± 0.5	42.85 ± 0.03	99.7 ± 0.0
NGC 5548	43.3 ± 0.19	43.58 ± 0.01	42.55 ± 0.01	134.3 ± 0.5	549 ± 28	42.28 ± 0.03	71.2 ± 4.9	41.76 ± 0.01	21.7 ± 0.4	42.17 ± 0.01	74.5 ± 0.4	41.65 ± 0.21	117.8 ± 0.2
PG 1426	44.63 ± 0.02	45.2 ± 0.01	43.72 ± 0.05	55.6 ± 6.0	208 ± 215	43.13 ± 0.05	20.3 ± 2.4	43.2 ± 0.05	18.2 ± 2.2	42.97 ± 0.04	21.9 ± 2.1	42.83 ± 0.04	80.1 ± 0.0
Mrk 817	43.74 ± 0.09	44.29 ± 0.01	42.82 ± 0.01	58.1 ± 0.7	357 ± 38	41.72 ± 0.25	7.0 ± 4.0	42.25 ± 0.01	17.4 ± 0.3	42.37 ± 0.05	58.9 ± 6.0	41.93 ± 0.14	78.5 ± 0.1
Mrk 1511	43.16 ± 0.06	43.48 ± 0.01	42.32 ± 0.03	112.0 ± 8.3	-245 ± 238	41.37 ± 0.15	15.4 ± 4.9	41.56 ± 0.09	25.9 ± 6.5	41.52 ± 0.06	115.5 ± 0.1
Mrk 290	43.17 ± 0.06	43.77 ± 0.01	42.71 ± 0.01	129.0 ± 1.8	321 ± 45	42.15 ± 0.13	39.0 ± 9.9	41.86 ± 0.04	18.3 ± 1.5	42.1 ± 0.01	54.9 ± 0.9	41.64 ± 0.06	153.0 ± 0.1
Mrk 486	43.69 ± 0.05	43.17 ± 0.02	41.88 ± 0.16	55.2 ± 15.3	-1110 ± 70	41.0 ± 0.21	5.5 ± 3.7	41.16 ± 0.09	9.7 ± 2.1	42.01 ± 0.07	41.6 ± 7.2	42.12 ± 0.04	135.9 ± 0.0
PG 1613	44.77 ± 0.02	45.18 ± 0.01	43.93 ± 0.01	88.7 ± 1.3	1117 ± 84	42.8 ± 0.18	9.6 ± 4.5	43.35 ± 0.02	49.6 ± 2.4	43.0 ± 0.03	86.		

Table 2
(Continued)

Objects	$\log \lambda L_{5100}$ (erg s^{-1})	$\log \lambda L_{1350}$ (erg s^{-1})	$\log L_{\text{CIV}}$ (erg s^{-1})	REW (C IV) (\AA)	C IV Blueshift (km s^{-1})	$\log L_{\text{CIII}}$ (erg s^{-1})	REW (C III) (\AA)	$\log L_{\text{HeII}1640}$ (erg s^{-1})	REW (He II 1640) (\AA)	$\log L_{\text{MgII}}$ (erg s^{-1})	REW (Mg II) (\AA)	$\log L_{\text{H}\beta}$ (erg s^{-1})	REW (H β) (\AA)	$\log L_{\text{He II } 4687}$	REW (He II 4687)
NGC 6814	42.12 \pm 0.28	41.66 \pm 0.02	40.61 \pm 0.03	182.6 \pm 11.7	-167 \pm 416	40.31 \pm 0.14	132.6 \pm 39.1	38.95 \pm 0.25	4.6 \pm 2.0	40.29 \pm 0.01	87.3 \pm 2.3	40.5 \pm 0.28	121.6 \pm 0.3
Mrk 509	44.19 \pm 0.05	44.62 \pm 0.01	43.49 \pm 0.01	116.7 \pm 0.9	344 \pm 31	43.12 \pm 0.03	65.2 \pm 4.7	42.55 \pm 0.05	14.5 \pm 1.6	42.86 \pm 0.01	49.7 \pm 0.7	42.61 \pm 0.04	132.7 \pm 0.0
NGC 7469	43.51 \pm 0.11	43.85 \pm 0.01	42.49 \pm 0.01	66.7 \pm 0.6	-253 \pm 40	41.79 \pm 0.06	16.4 \pm 2.1	41.93 \pm 0.02	19.3 \pm 1.1	42.1 \pm 0.01	50.2 \pm 1.7	41.6 \pm 0.1	63.0 \pm 0.1
Zw 229	42.71 \pm 0.05	43.16 \pm 0.01	42.25 \pm 0.04	187.0 \pm 20.8	870 \pm 485	41.37 \pm 0.04	28.1 \pm 2.7	41.16 \pm 0.37	16.1 \pm 13.8	41.52 \pm 0.01	49.6 \pm 1.6
Mrk 1501	44.32 \pm 0.05	44.7 \pm 0.01	43.61 \pm 0.01	120.3 \pm 3.0	-108 \pm 88	43.18 \pm 0.13	48.6 \pm 10.9	43.08 \pm 0.07	36.0 \pm 4.8	42.99 \pm 0.05	35.0 \pm 3.6
Mrk 50	42.88 \pm 0.07	43.22 \pm 0.01	42.16 \pm 0.02	152.6 \pm 6.4	-57 \pm 86	41.01 \pm 0.16	14.4 \pm 7.6	41.4 \pm 0.01	45.4 \pm 0.7
NGC 4395	39.77 \pm 0.02	39.82 \pm 0.01	38.62 \pm 0.05	82.9 \pm 11.5	1187 \pm 544	37.83 \pm 0.02	14.0 \pm 0.6
Mrk 6	43.75 \pm 0.06	42.09 \pm 0.1	40.9 \pm 0.16	91.0 \pm 29.6	4497 \pm 2534	40.33 \pm 0.18	22.5 \pm 10.5	40.44 \pm 0.08	31.3 \pm 5.5	40.94 \pm 0.04	64.7 \pm 6.3

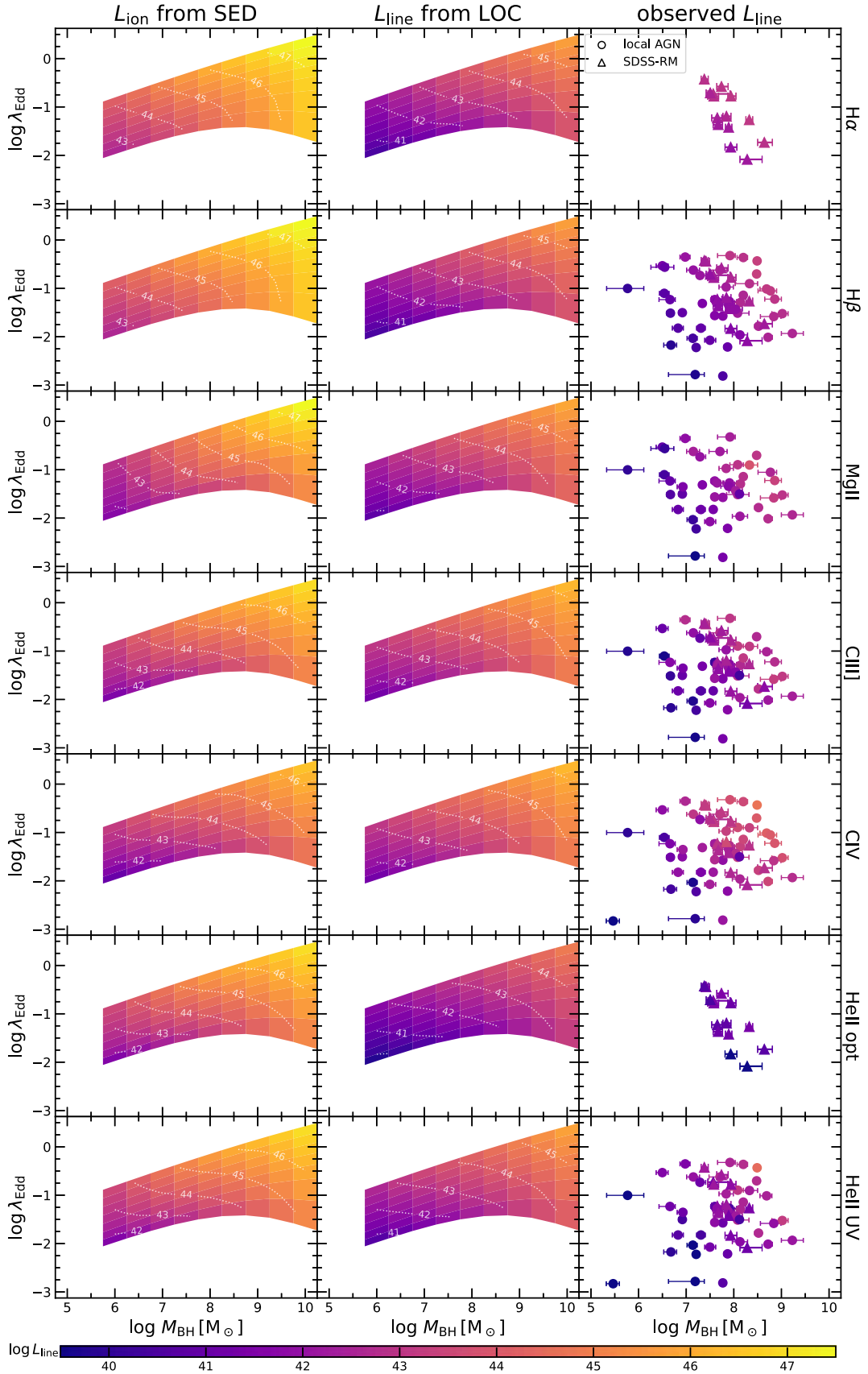


Figure 8. Distributions of line luminosities in the $M_{\text{BH}}-\lambda_{\text{Edd}}$ plane. The left panels show the integrated ionizing luminosity ($L_{\text{ion}} = \int_{\nu_{\text{product}}}^{\nu_{\text{destruct}}} L_{\nu} d\nu$ within the production and destruction photon energies), the middle panels display the line luminosities predicted by the LOC model, and the right panels present the observed line luminosities as a visual assessment of the theoretical photoionization. The increasing trend in all panels demonstrates the consistency between our theoretical computations and observations.

observations suggests that our observed emission line flux can be explained by the simple LOC model and depends on the BH parameters and subsequently the ionizing SEDs. For even lower accretion rates ($\log \dot{m} < -1.5$), the computational limitations of `qsos` restrict us from evaluating the incident continuum and subsequently performing photoionization computations.

We also compare theoretical and observed rest-frame equivalent widths (EWs) of several emission lines as functions of BH mass and Eddington ratio in Figure 9. In the left panels, we use the incident SED and LOC-predicted line flux to predict the EW. For massive BHs ($M_{\text{BH}} > 10^8 M_{\odot}$), more luminous (higher accretion rate) BHs exhibit weaker emission line strength, particularly for UV lines, and vice versa for BHs with mass $M_{\text{BH}} \leq 10^8 M_{\odot}$, as predicted by the LOC model. This pattern predicted by the LOC model indicates that the continuum and line luminosities change nonlinearly with M_{BH} and λ_{Edd} . This nonlinear relationship suggests that the underlying SED shape may be more complex and varies significantly with changes in these parameters. The middle panels of Figure 9 show the observed EW values, and the right panels display binned observed EW values. The Baldwin effect could be observed, as the higher-accretion and more massive objects show lower EWs in all three panels. Although the predicted EWs in C III], He II $\lambda 4687$, and He II $\lambda 1640$ are slightly higher than observed, the overall observed EW values remain generally consistent with the predictions from the LOC model. This consistency is expected as the observed continuum luminosities and line flux agree with the prediction in Figures 4 and 8, respectively. However, due to sample selection biases for the RM AGNs (i.e., missing low-mass, low accretion rate objects), it is difficult to explore the EW in the lower left corner of the $M_{\text{BH}}-\lambda_{\text{Edd}}$ space; thus, we are unable to demonstrate the same diagonal trend in the LOC model prediction.

3.3. Comparisons of Composite UV Spectra

Since observed (and measured) properties in individual objects can suffer from significant measurement uncertainties, we also use the higher-S/N composite spectra to compare with theoretical predictions. Figure 10 presents the composite rest-frame UV spectra for RM AGNs within a matched optical luminosity range ($43 \leq \log(\lambda L_{5100}) \leq 45$) but with different λ_{Edd} (top panel) and $H\beta$ lags (bottom panel). The fluxes are normalized at rest-frame wavelength 1350 Å to better illustrate the UV line strength. In the top panel, subsets with higher λ_{Edd} values (green) exhibit stronger Ly α line strengths compared to the lower accretion group (blue). According to the SED example in Figure 3 and our photoionization results in Figure 9, at a matched optical luminosity, BHs with higher accretion rates possess more ionizing energy for both hydrogen and C IV, resulting in stronger emission lines. This trend is evident in our composite spectra, where higher accretion rate samples tend to show stronger emission lines. This agreement demonstrates that our photoionization models can accurately generate line strengths based on the given BH parameters.

Likewise, in the bottom panel of Figure 10, we divide our sample into two subsets based on their $H\beta$ time lag relative to the canonical $R-L$ relation. The subset with lags shorter than the $R-L$ relation (green) has stronger C IV line strength compared to the longer-lag subset (blue), while these two spectra appear to have similar Ly α line strength. Given that C IV is a collisionally excited line with an excitation energy of

8 eV, the shorter-lag subset suggests that it may have an additional ionizing flux at far-UV compared to the longer-lag subset, with the former corresponding to the higher-accreting systems in Figure 3. However, it appears to contradict our BLR size prediction in Figure 5 that higher-accreting objects should have more ionizing energy and thus longer lags. This discrepancy may be due to the constant parameters of our BLR size prediction, which will be discussed further in Section 4.2.

4. Discussion

4.1. Line Ratios as a Proxy for SED Shape

Our LOC model photoionization calculations have shown qualitative agreement with the observed line properties (line strengths, BLR distances, etc.). Since lines with different ionization potentials depend on different parts of the SED, it is desirable to infer the underlying ionizing SED (not directly observable) from observables, such as the flux ratios between low- and high-ionization lines.

Figure 11 displays several groups of continuum luminosity ratios and line flux ratios as functions of M_{BH} and λ_{Edd} , predicted from photoionization calculations. In the top panels of Figure 11, the monochromatic luminosities at the ionizing energies of C IV (64.5 eV), Mg II (15.0 eV), $H\beta$ (13.6 eV), and He II $\lambda 1640$ (54.4 eV) are computed from the grid of SEDs, and then their line ratios are placed in the $M_{\text{BH}}-\lambda_{\text{Edd}}$ plane. The bottom panels show the corresponding line luminosity ratios of the same lines as in the top panels. The line luminosity ratio is computed using `CLOUDY` and the LOC model, as explained in Section 2.2. Both monochromatic luminosity ratios and line luminosity ratios demonstrate a complicated dependence on the mass and accretion rate. Given that C IV and Mg II are collisionally excited lines with excitation energies of 8 and 4.4 eV, while $H\beta$ and He II $\lambda 1640$ are recombination-dominated lines, the line ratios involving C IV may not accurately trace the SED shape, especially at the high-mass, low-accretion end; in contrast, He II $\lambda 1640$ is more effective in tracing the SED shape in Figure 11.

Given the strong correlations between predicted continuum luminosity ratios and line flux ratios in Figure 11, we use the BH mass M_{BH} , accretion rate λ_{Edd} , and line flux ratios in our theoretical computation models to provide empirical relations that map the underlying ionizing SED shape from ~ 10 to ~ 60 eV. The concept of using UV emission line strengths to probe the ionizing SED has been previously applied to the EW of He II $\lambda 1640$ as tracers of the EUV continuum (e.g., W. G. Mathews & G. J. Ferland 1987; K. T. Korista & M. R. Goad 2000; K. M. Leighly 2004; M. J. Temple et al. 2023). However, this approach does not consider the possibility that the ionizing continuum that the BLR gas receives is not the same as what observers see; thus, the He II $\lambda 1640$ EW is not tracing the real ionizing continuum shape but the ratio between ionizing energy for He II $\lambda 1640$ and the continuum that the observer receives (J. D. I. Timlin et al. 2021). To address this issue, we use the flux ratio of different UV/optical line pairs to directly map the underlying SED shape, which involves only the ionizing continuum received by the BLR gas.

To demonstrate the ability of observables to trace the SED shape with empirical relations, we use linear regression to fit

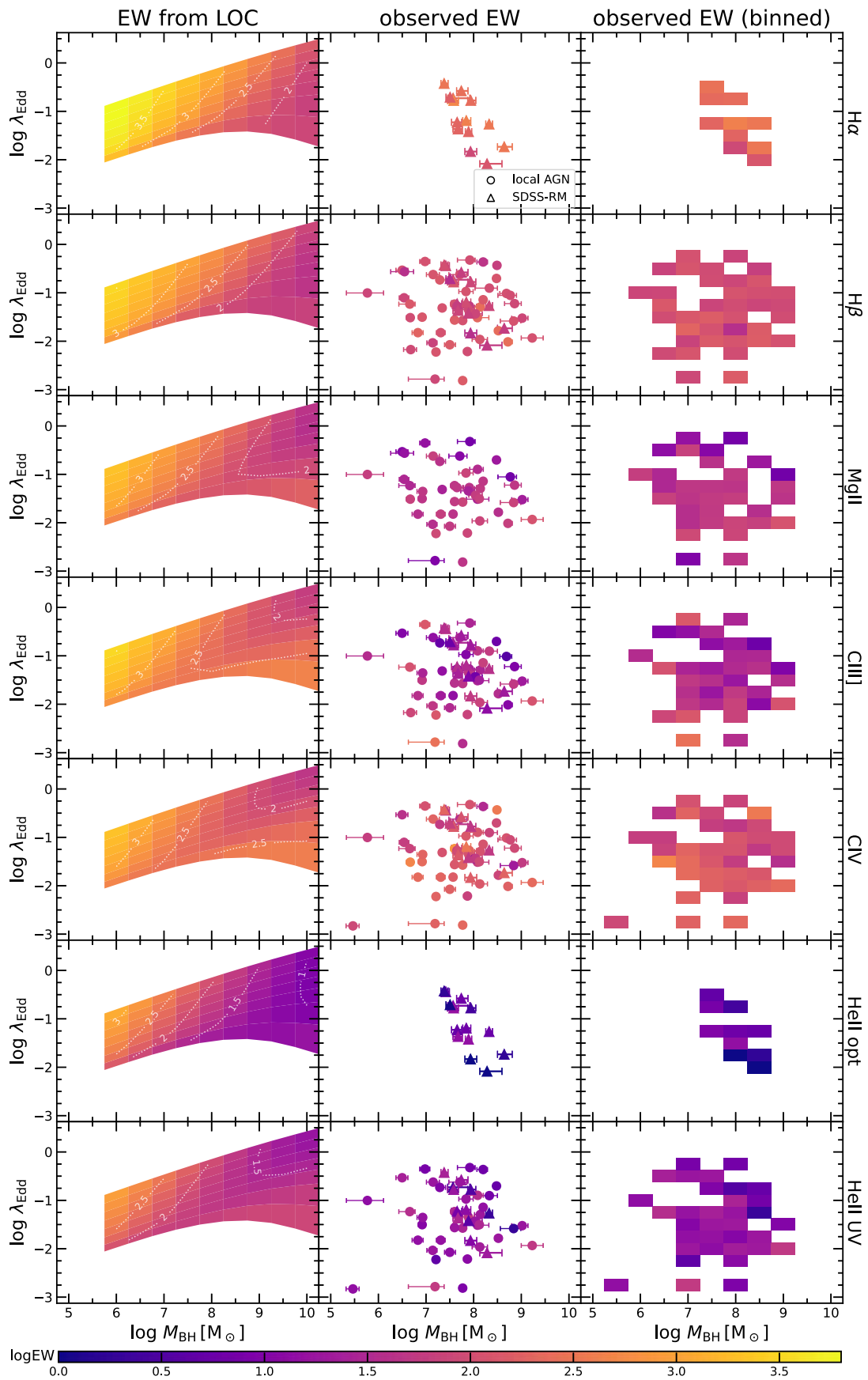


Figure 9. Distributions of emission line EW in the $M_{\text{BH}}-\lambda_{\text{Edd}}$ plane. The left panels display the EW distributions predicted by the LOC model. The middle panels present the observed EW from the AGN sample, and the right panels display the binned EW.

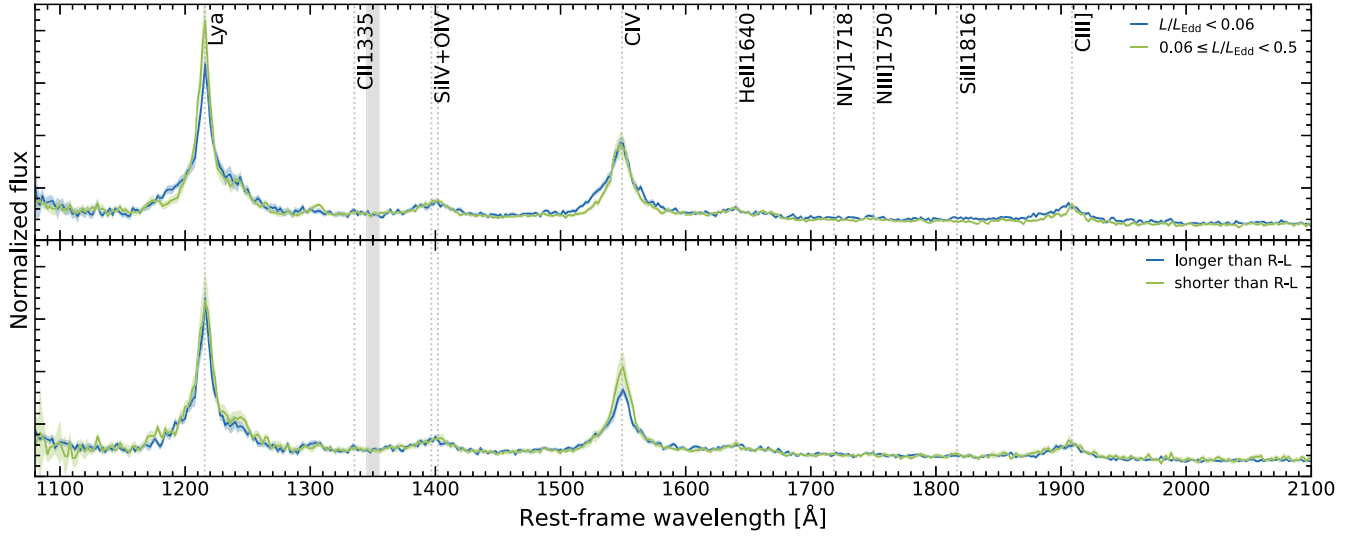


Figure 10. Median composite spectra for different accretion rate samples (top) and different $H\beta$ lag samples (bottom) with roughly matched optical luminosity $43 \leq \log(\lambda L_{5100}) \leq 45$, normalized at 1350 \AA (gray shaded area).

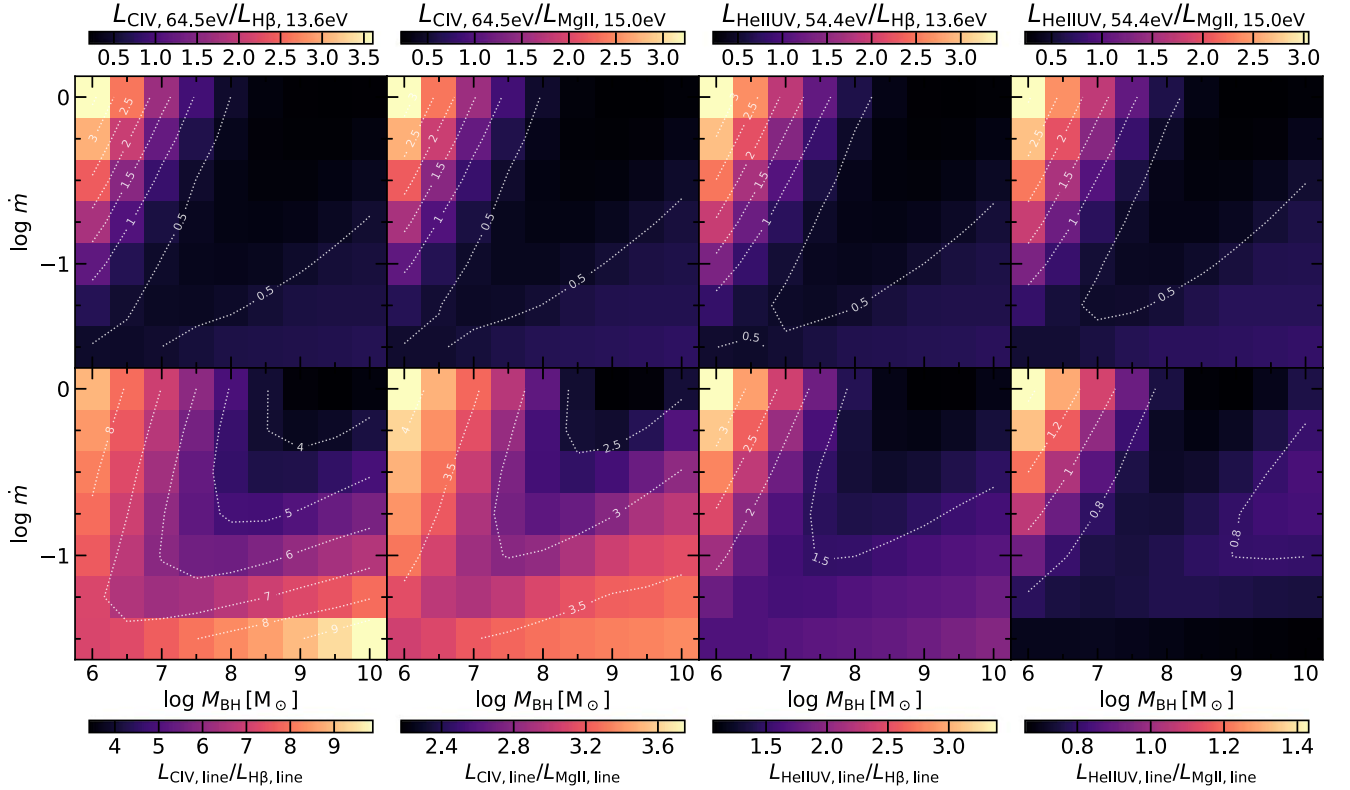


Figure 11. Contour plots illustrating the dependence of monochromatic luminosity ratios at selected energies (top panels) and various predicted emission line ratios (bottom panels) on both BH mass and accretion rate. The top panels reflect the underlying SED shape, while the bottom panels show how the BLR clouds respond to different SEDs. Comparing the two rows, He II $\lambda 1640$ is more effective in tracing the SED shape.

the theoretical results with the following relation:

$$\log(L_{E_1}/L_{E_2}) = \theta_0 + \theta_1 \log M_{\text{BH}} + \theta_2 \log \lambda_{\text{Edd}} + \theta_3 \log(L_{\text{line1}}/L_{\text{line2}}), \quad (5)$$

where L_E is the monochromatic luminosity at energy E and E_1 and E_2 are the ionizing energy of line 1 and line 2, respectively. The best-fit parameters are listed in Table 3. The scaling

relations between the observables and the ionization continuum shape are shown in Figure 12. The coefficients ($R^2 = 1 - \sum_{i=1}^n (y_i - \hat{y}_i)^2 / \sum_{i=1}^n (y_i - \bar{y})^2$) of the four pairs of lines suggest that the line ratios can trace the ionizing continuum shape at $\sim 10 \text{ eV}$ fairly well, especially for C IV/Mg II.

Multiwavelength observations probing additional emission lines with different ionizing energies will allow mapping the ionizing continuum to an even wider range. For example, the

Table 3Best-fit Parameters of Line Excitation Energy Ratios $\log(L_{E_1}/L_{E_2})$ Defined in Equation (5)

Line Ratios	θ_0	θ_1	θ_2	θ_3
C IV/H β	-0.894	-0.169	0.567	3.163
C IV/Mg II	-1.602	-0.109	0.335	5.362
He II λ 1640/H β	-0.327	-0.045	0.106	2.535
He II λ 1640/Mg II	-0.451	0.040	-0.257	3.163

line ratios of infrared coronal lines (CLs) from different elements and different excitation states have proven to be related to the intrinsic BH properties (M_{BH} and \dot{m}), chemical abundance, and ionization parameters (J. W. Ferguson et al. 1997). Most importantly, CLs have the capability to map the ionizing continuum to energy levels exceeding 100 eV, making these data more powerful than UV data alone. Photoionization computations in J. M. Cann et al. (2018) demonstrate that several pairs of CL ratios might trace intermediate-mass BHs in dwarf galaxies, as the harder SEDs in intermediate-mass BHs can excite stronger high-ionization lines. With the advent of the James Webb Space Telescope, infrared spectroscopic observations covering a wealth of IR CLs will provide a viable approach to studying the connections between the ionizing continuum and CL emission and to understanding the physical driver of the diversity in quasar line strength.

4.2. Dispersion in the H β R–L Relation

In Section 2.3, we predicted the H β time lags with constant ionization parameter and compared them with the observed lags. Since the BLR is sensitive to the entire ionizing flux emitted by the central source, varying M_{BH} and λ_{Edd} leads to different ionizing SEDs that are responsible for different BLR sizes as well as different line-ionizing fluxes for different line-emitting ions in the BLR clouds. The parameters (M_{BH} and λ_{Edd}) are degenerate at fixed optical luminosity in the R–L relation, as shown in Figures 3 and 4. It is therefore natural to expect an intrinsic dispersion in time lags at fixed optical luminosity caused by different accretion parameters and subsequently the underlying SED. So far, this model has been the most favored interpretation in recent work on this topic (B. Czerny et al. 2019; P. Du & J.-M. Wang 2019; M. L. Martínez-Aldama et al. 2019; E. Dalla Bontà et al. 2020; G. Fonseca Alvarez et al. 2020; Y. Shen et al. 2024). Moreover, smearing our theoretical predictions with observed uncertainties demonstrates that uncertainties in the measured time lag along with luminosity variability can introduce additional scatter in the R–L relation.

The scale of the BLR can also be affected by other accretion parameters that were not included in this preliminary study. For example, in the high-accretion regime (approaching the Eddington limit), the accretion disk structure may significantly depart from the SSD model (N. I. Shakura & R. A. Sunyaev 1973) and become a slim disk (M. A. Abramowicz et al. 1988), where the disk scale height is comparable to the radius. The slim disk geometry will produce anisotropic radiation fields due to the self-shadowing effect, which could reduce the ionizing flux and soften the SED that the BLR cloud receives. In particular, systematically shorter H β time lags in high-accretion quasars have been reported by the SEAMBH collaboration (P. Du et al. 2014, 2015; P. Du et al. 2018; C. Hu et al. 2021). Due to considerable theoretical uncertainties in the slim disk

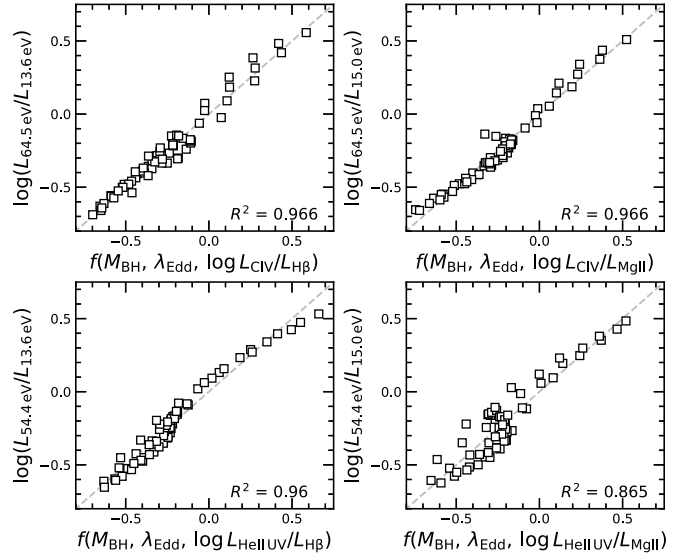


Figure 12. Scaling relations of monochromatic luminosity ratios (i.e., SED shape) and observables (M_{BH} , λ_{Edd} , and line flux ratio) for the theoretical models, with the coefficients of determination R^2 in the upper left corners.

SED predictions and the relative paucity of UV spectroscopy for RM AGNs accreting in this regime, we defer a more complete investigation of AGNs with slim disk accretion to a future paper.

It is important to note, however, that our investigations suggest that in the low-to-moderate-accretion thin-disk regime, the BLR time lag exhibits a strong dependence on both the BH mass and accretion rate. As demonstrated in Figure 5, an increase in either the BH mass or accretion rate leads to a corresponding increase in both the optical luminosity and the time lag, and the accretion rate has a more significant impact on the lag than the BH mass. This prediction, however, is in tension with the observed lag dispersion at fixed optical luminosity, suggesting that additional factors may influence the observed lags. Figure 13 illustrates the observed R–L relation for our RM AGN sample (left panel) and highlights how the Eddington accretion rate influences the H β lag across different optical luminosities (right). The data points are divided into eight groups based on their optical luminosity λL_{5100} , with observed data points within each group color-coded according to their relative Eddington ratio in each bin. Even within the SSD regime analyzed in this study, a subtle decreasing trend in H β lags is observed as L/L_{Edd} increases in each luminosity bin. While our model does not explore a broad parameter space in the right panels, it nonetheless predicts an increasing H β lag with higher L/L_{Edd} . This discrepancy suggests that certain simple assumptions in our photoionization modeling, e.g., a universal gas density, might be incorrect. For example, if n_{H} increases with L/L_{Edd} , and given that $R_{\text{BLR}} \propto n_{\text{H}}^{-1/2}$ (Equation (4)), we expect a more compact BLR size from the LOC model, which would be more consistent with the observed trend in the R–L plane. Additionally, as n_{H} increases, broad-line emissivity would also increase, resulting in even higher predicted broad-line fluxes for higher Eddington ratios, again consistent with observations. Other choices of photoionization parameters or assumptions may also yield alternative R–L trends, which we leave for future studies to further explore these dependencies.

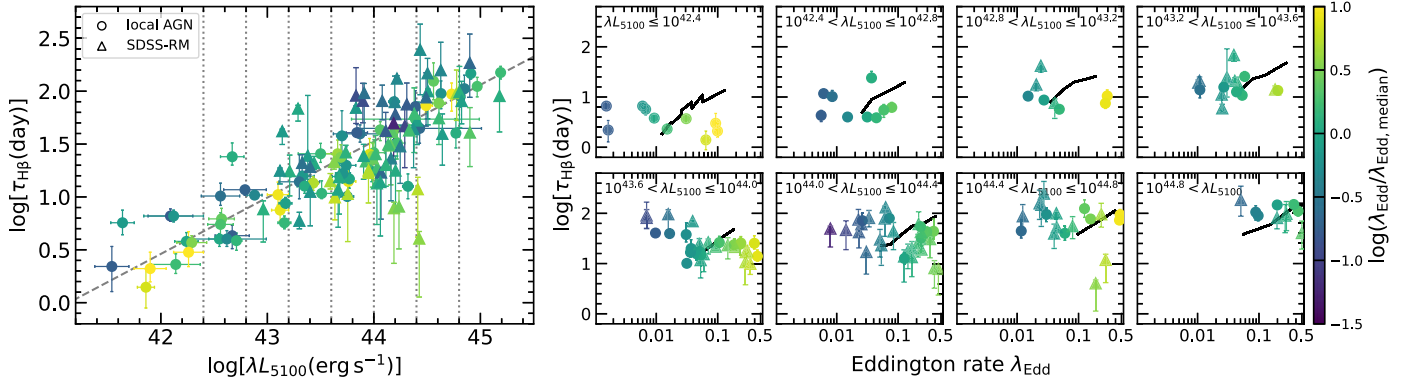


Figure 13. Left: the R - L relation showing the observed $H\beta$ lag vs. optical luminosity for reverberation-mapped AGNs with $\lambda_{\text{Edd}} < 0.5$, divided into eight groups based on their optical luminosity (indicated by gray dotted lines). Right: the observed (circles and triangles) and predicted (black lines) $H\beta$ lag as a function of the Eddington accretion rate for each luminosity group identified in the left panel. In both panels, the observed data points are color-coded according to the relative $\log \lambda_{\text{Edd}}$ values, calculated as the ratio of the λ_{Edd} value to the median λ_{Edd} within each λL_{5100} bin.

Table 4

Best-fit Parameters of the Hydrogen-ionizing Photon Flux $\log Q(\text{H})$ in Equation (6)

Line Ratios	θ_0	θ_1	θ_2	θ_3
C IV/ $H\beta$	53.035	0.475	1.636	0.358
C IV/Mg II	53.140	0.479	1.581	0.200
He II $\lambda 1640/H\beta$	53.057	0.492	1.583	0.342
He II $\lambda 1640/Mg II$	53.119	0.493	1.546	0.282

4.3. Predicted Hydrogen-ionizing Photon Flux

In our theoretical analysis, the time lag of $H\beta$ is modeled as a linear function of the hydrogen-ionizing photon flux $Q(\text{H})$, as expressed by Equation (4). Because the observed ionizing continuum may not be the same as the BLR receives, the flux ratios of emission lines from species with different ionization potentials are the most promising way to constrain the ionizing photon flux that directly determines the BLR size (C. A. Negrete et al. 2012; G. J. Ferland et al. 2020; T. M. Buendia-Rios et al. 2023). As discussed in Section 4.1, the line flux ratios, coupled with the mass and Eddington ratio, have demonstrated their potential in deriving the SED shape. Therefore, we adopt a similar approach to predict the $Q(\text{H})$ for observed quasars through the following equation:

$$\log Q(\text{H}) = \theta_0 + \theta_1 \log M_{\text{BH}} + \theta_2 \log \lambda_{\text{Edd}} + \theta_3 \log(L_{\text{line1}}/L_{\text{line2}}). \quad (6)$$

We first fit a linear regression relation on the parameter grid derived from theoretical models, and the best-fit parameters are listed in Table 4. The linear regression scaling is shown in Figure 14 for the four line pairs, where the ionizing photon flux $Q(\text{H})$ could be well estimated using such observables (M_{BH} , λ_{Edd} , and line flux ratios).

Subsequently, we apply the regression parameters to the observed RM quasars. Figure 15 presents the color-coded R - L relation for low-accretion AGNs with their predicted $Q(\text{H})/\lambda L_{5100}$ value. Since our assumption in Section 2.3 implies that $R_{\text{BLR}} \sim Q^{0.5}$, suggesting that at any given λL_{5100} , $H\beta$ lags would follow a vertical increase as $Q(\text{H})/\lambda L_{5100}$, such a vertical trend can be seen in Figure 15. However, in Figure 13, $H\beta$ lags show a decreasing trend as relative accretion rates increase, suggesting the opposite trend to

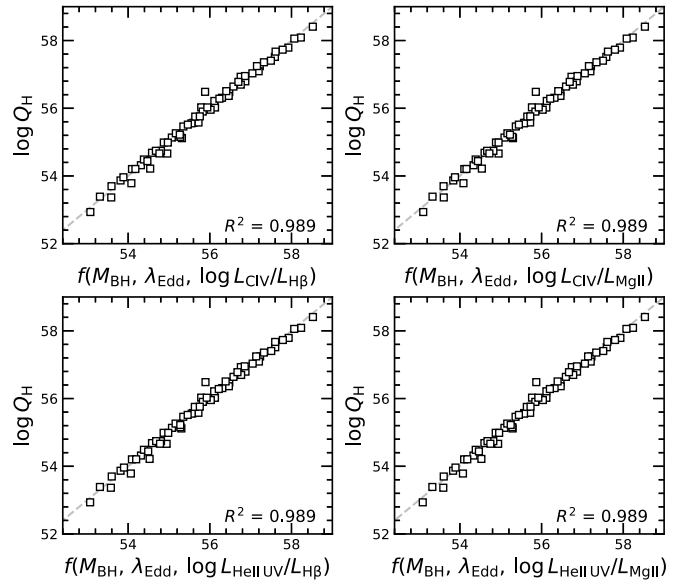


Figure 14. Linear regression scaling between the ionizing photon number $Q(\text{H})$ and the observables for theoretical measurements.

Figure 15. This discrepancy is possibly due to oversimplified assumptions (e.g., the constant hydrogen density) in our BLR size prediction (see Section 4.2).

4.4. Uncertainties and Limitations

The primary goal of this paper is to explore the first-order effects of varying the BH mass and accretion rate on the BLR distance and the diverse line strengths within the LOC model framework. While the success of the LOC model in previous studies is often attributed to its flexibility in determining photoionization parameters (e.g., $n(\text{H})$, U_{H} , and the covering factor) on a case-by-case basis for a small number of objects (e.g., K. T. Korista & M. R. Goad 2000, 2004), our goal is to investigate broader trends across a representative AGN population. The use of predetermined LOC model parameters in our approach allows for a more generalized statistical analysis, which is necessary to capture the impact of BH parameters on the observables for the AGN population studies. The parameters adopted in this study are well tested by multiple previous studies (e.g., W. G. Mathews & G. J. Ferland 1987;

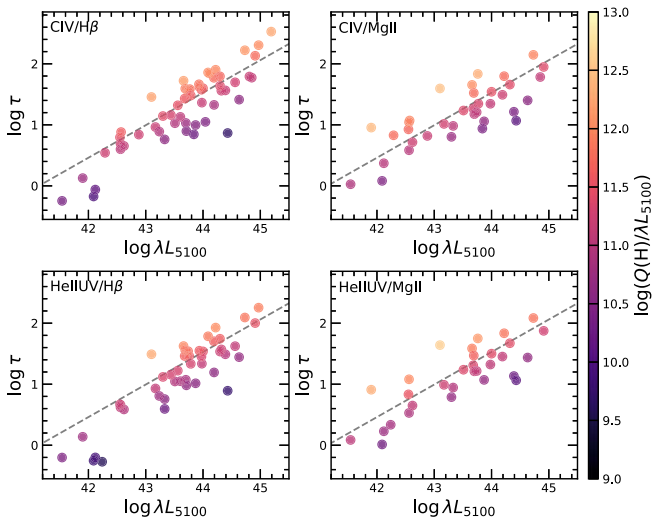


Figure 15. Predicted $H\beta$ time lag following Equation (4) vs. the observed optical luminosity, color-coded by $Q(H)/\lambda L_{5100}$, where the ionizing photon flux $Q(H)$ is predicted from observed parameters (Equation (6)).

K. T. Korista & M. R. Goad 2004, 2019; H. Guo et al. 2020). We emphasize that we have not attempted to construct a model finely tuned to match the properties of any specific AGN. This general approach quantitatively reproduces the behavior of the BLR distance and line luminosity relative to BH mass and accretion rate given universal ionization parameters. However, this photoionization modeling is carried out for low-accretion quasars in the SSD regime with fixed inclination $\cos i = 0.5$ and for nonspinning BHs only. The impact of BH spin on the BLR size is pronounced, which would affect the shape of the ionizing continuum, especially in the UV band (J.-M. Wang et al. 2014a; A. Kubota & C. Done 2018; C. S. Reynolds 2021). The inclusion of BH spin in our analysis would introduce additional complexity, potentially leading to a greater dispersion in the R - L relation (B. Czerny et al. 2019) and producing degenerating results with BH mass and accretion rate.

In our SED modeling, because of the imposed accretion rate limits of $-1.65 < \log \dot{m} < 0.39$ in q_{sosed} , this work is limited to mostly the SSD-dominated accretion regime and only models $\log \dot{m} \leq 0$. Compared to the original agn_{sed} , the simplified model q_{sosed} fixes the electron temperature and spectral index at typical values for the warm and hot Comptonization components as follows: $kT_{\text{e,hot}} = 100$ keV, $kT_{\text{e,warm}} = 0.2$ keV, $\Gamma_{\text{warm}} = 2.5$, $r_{\text{warm}} = 2r_{\text{hot}}$, $r_{\text{out}} = r_{\text{sg}}$, $h_{\text{max}} = 100$, with the power dissipated by the hot Comptonization region fixed at $0.02L_{\text{Edd}}$ (A. Kubota & C. Done 2018). By comparing the stacked AGN SEDs from SOUX (D. Kynoch et al. 2023) with q_{sosed} predictions, J. A. J. Mitchell et al. (2023) found that while the q_{sosed} model matches well with the observed SEDs for intermediate-mass AGNs ($\log M_{\text{BH}} = 7.5 - 9.0$), it underpredicts the X-ray flux at low M_{BH} and shows discrepancies in the optical/UV continuum for high- M_{BH} AGNs. Assuming that the X-ray emission is generated from the hot Comptonization region and the EUV emission originates from the warm Comptonization region (A. Kubota & C. Done 2018; P. O. Petrucci et al. 2018), the absence of a predictive model with a solid theoretical basis to untangle the poorly understood warm Comptonization component and its relation to the hot Comptonization coronal properties still limits the comparison between observations and

theoretical analysis and thereby our understanding of AGN SEDs. However, the demonstrated correlations between the X-ray, EUV, and UV regions (e.g., P. J. Green 1996; A. T. Steffen et al. 2006; D. W. Just et al. 2007; E. Lusso & G. Risaliti 2016; J. D. Timlin et al. 2020; J. D. I. Timlin et al. 2021) may provide crucial insights that could uncover the nature of the hot/warm corona in quasars. Despite that this simplified q_{sosed} model may provide limited flexibility in SED shapes, our LOC photoionization computations indicate that this straightforward model can successfully reproduce the line strengths as observed for various BH mass and accretion rates. As discussed in Section 4.2, as the accretion rate substantially increases beyond the SSD-dominated regime, the accretion disk solution may be better described by the slim disk model with a puffed-up inner disk that shadows outer regions, which will potentially soften the SED received by the BLR clouds (M. A. Abramowicz et al. 1988; J.-M. Wang et al. 2014b). Due to the complexities involved in modeling such a scenario and the uncertainties in slim disk SED prediction, we postpone a comprehensive investigation of these high-accretion AGNs to future work.

While we demonstrate the potential of using line ratios to probe the SED shape and the ionizing flux, the predicted line ratios may deviate from observed line ratios. This discrepancy can arise from factors such as differences in metallicity and assumptions regarding various ionizing conditions (K. T. Korista & M. R. Goad 2019; S. Panda et al. 2019). For instance, the radiative pressure confinement (RPC) model (A. Baskin et al. 2014) offers an alternative BLR structure by assuming that the radiation pressure confines photoionized gas, leading to a universal $U \sim 0.1$ and $n(H) \sim 10^{11}$ for the inner layer, independent of distance and luminosity. Under RPC conditions, the predicted R - L trend remains unchanged since only the product of U and $n(H)$ influences the scaling in Equation (4), which cannot explain the shorter lags for high-accretion AGNs. Although the gas is not at its highest emissivity at such U and $n(H)$, the constraints on the photoionization parameters make the line flux ratio more dependent on the incident SED shape compared to the LOC model. Although mechanisms other than BH mass and accretion rate will have some effects on the BLR size and observed line strength, we have demonstrated that variations in the $M_{\text{BH}}-\lambda_{\text{Edd}}$ have successfully reproduced the lags and emission line properties over many orders of magnitude in luminosity and BH mass. Nevertheless, discrepancies remain in the detailed predictions of the lag dispersion at fixed optical luminosity, as discussed in Section 4.2.

There is the possibility that the BLR gas sees a different ionizing continuum than the observer, due to a potential inner shielding gas component that blocks the ionizing X-ray and EUV continuum (e.g., J. Wu et al. 2011, 2012; B. Luo et al. 2015; R. M. Plotkin et al. 2015; Q. Ni et al. 2018, 2022). In this self-shielding gas model, the disk component (< 1 keV) in the incident SED is reduced by the shielding gas (J.-M. Wang et al. 2014b), whereas the warm and hot Comptonized components are not affected much. Consequently, the hydrogen-ionizing photon flux $Q(H)$ is reduced as well. Given that $Q(H) \propto \Phi R^2$ (Equation (4)), this reduction means that, compared to our LOC model, gas at a fixed distance (R) would have a lower surface ionizing flux Φ , and gas with the same Φ would reside closer to the center. As a result, the overall line emission from the BLR would be reduced, and the BLR clouds would be more

concentrated toward the center in this shielding gas model. In this work, we do not observe much evidence for this shielding gas component, as the predicted line strengths are consistent with the BLR seeing all the continuum flux. However, the covering fraction (G. J. Ferland et al. 2020) and the impact of this shielding gas may become more prominent for even higher Eddington ratios, where the inner region of the slim disk may be geometrically thicker. Due to the complexity of modeling self-shielded SEDs, we plan to investigate this possibility in future work.

5. Conclusions

In this paper, we have performed CLOUDY photoionization calculations with the empirical LOC model and typical parameters to predict the broad-line emission as functions of accretion parameters, BH mass, and accretion rate using the latest AGN SED models (A. Kubota & C. Done 2018) as the input continuum. We compare our theoretical results with observed AGN properties for a sample of 67 low-redshift AGNs with RM measurements that are in the sub-Eddington accretion regime. Our main conclusions are as follows.









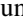



1. Assuming universal values of hydrogen density ($\log n(\text{H}) = 12$) and ionization parameter ($\log U_{\text{H}} = -2$), the photoionization models reproduce the observed global relation between the Balmer broad-line lag and optical luminosity at rest-frame 5100 Å (Section 2.3). However, at fixed L_{5100} , the model predicts longer lags for higher Eddington ratios, opposite to the observed trend (Figure 13). This discrepancy implies that the assumption of constant gas density may not be realistic, or that other factors are at play, such as a self-shielding wind in high-Eddington-ratio AGNs that significantly reduces the ionizing flux seen by the BLR (Sections 4.2 and 4.4).
2. The photoionization models produce increasing optical and UV broad-line strengths with accretion rate at fixed BH mass or optical luminosity, which are consistent with observations. Overall, the distributions of different broad-line fluxes in the $M_{\text{BH}}-\lambda_{\text{Edd}}$ plane are consistent between observations and theoretical predictions (Section 3.2).
3. Based on these comparisons, we provide empirical scaling relations (Equations (5) and (6)) that utilize the observed BH mass, L/L_{Edd} , and line flux ratios to constrain the ionizing continuum flux, which is not directly observable (Section 4.3).

The overall consistency between observations of AGN broad-line properties and photoionization modeling suggests that such analyses are important to fully decipher the accretion parameters and the resulting broad-line emission in broad-line AGNs. The optical and UV broad emission lines only sample a limited portion of the ionizing continuum, and future observations with high-ionization CLs (with ionizing energy at $>150\text{ eV}$) can lead to better constraints on the overall continuum SED. Further refinements of the LOC model and AGN continuum models, as well as extending to higher accretion rates better described by the slim disk model, will be crucial to fully understanding the dispersion of lags at fixed optical luminosity, an important step to designing more accurate single-epoch BH mass recipes using the $R-L$ relation.

Acknowledgments

We thank the referee for a thorough report and many suggestions that greatly improved this work. Q.W. and Y.S. acknowledge partial support from NSF grant AST-2009947. Based on observations with the NASA/ESA Hubble Space Telescope obtained from the Data Archive at the Space Telescope Science Institute, which is operated by the Association of Universities for Research in Astronomy, Incorporated, under NASA contract NAS5-26555. Support for programs HST-GO-16171 and HST-GO-17433 was provided through a grant from the STScI under NASA contract NAS5-26555. H.X. G. is supported by the National Key R&D Program of China No. 2022YFF0503402, 2023YFA1607903. L.C.H. was supported by the National Science Foundation of China (11991052, 12233001), the National Key R&D Program of China (2022YFF0503401), and the China Manned Space Project (CMS-CSST-2021-A04, CMS-CSST-2021-A06). J.L.L. is supported by the Eric and Wendy Schmidt AI in Science Postdoctoral Fellowship, a Schmidt Futures program.

ORCID iDs

Qiaoya Wu  <https://orcid.org/0000-0003-4202-1232>
 Yue Shen  <https://orcid.org/0000-0003-1659-7035>
 Hengxiao Guo  <https://orcid.org/0000-0001-8416-7059>
 Scott F. Anderson  <https://orcid.org/0000-0002-6404-9562>
 W. N. Brandt  <https://orcid.org/0000-0002-0167-2453>
 Catherine J. Grier  <https://orcid.org/0000-0001-9920-6057>
 Patrick B. Hall  <https://orcid.org/0000-0002-1763-5825>
 Luis C. Ho  <https://orcid.org/0000-0001-6947-5846>
 Yasaman Homayouni  <https://orcid.org/0000-0002-0957-7151>
 Keith Horne  <https://orcid.org/0000-0003-1728-0304>
 Jennifer I-Hsiu Li  <https://orcid.org/0000-0002-0311-2812>
 Donald P. Schneider  <https://orcid.org/0000-0001-7240-7449>

References

- Abramowicz, M. A., Czerny, B., Lasota, J. P., & Szuszkiewicz, E. 1988, *ApJ*, **332**, 646
- Abuter, R., Allouche, F., Amorim, A., et al. 2024, *Natur*, **627**, 281
- Arnaud, K. A. 1996, in ASP Conf. Ser. 101, *Astronomical Data Analysis Software and Systems V*, ed. G. H. Jacoby & J. Barnes (San Francisco, CA: ASP), 17
- Baldwin, J., Ferland, G., Korista, K., & Verner, D. 1995, *ApJL*, **455**, L119
- Barth, A. J., Bennert, V. N., Canalizo, G., et al. 2015, *ApJS*, **217**, 26
- Baskin, A., Laor, A., & Stern, J. 2014, *MNRAS*, **438**, 604
- Bentz, M. C., & Katz, S. 2015, *PASP*, **127**, 67
- Bentz, M. C., Denney, K. D., Grier, C. J., et al. 2013, *ApJ*, **767**, 149
- Blandford, R. D., & McKee, C. F. 1982, *ApJ*, **255**, 419
- Blanton, M. R., Bershad, M. A., Abolfathi, B., et al. 2017, *AJ*, **154**, 28
- Boroson, T. A., & Green, R. F. 1992, *ApJS*, **80**, 109
- Buendia-Rios, T. M., Negrete, C. A., Marziani, P., & Dultzin, D. 2023, *A&A*, **669**, A135
- Cann, J. M., Satyapal, S., Abel, N. P., et al. 2018, *ApJ*, **861**, 142
- Castelló-Mor, N., Netzer, H., & Kaspi, S. 2016, *MNRAS*, **458**, 1839
- Czerny, B., Wang, J.-M., Du, P., et al. 2019, *ApJ*, **870**, 84
- Dalla Bontà, E., Peterson, B. M., Bentz, M. C., et al. 2020, *ApJ*, **903**, 112
- Done, C., Davis, S. W., Jin, C., Blaes, O., & Ward, M. 2012, *MNRAS*, **420**, 1848
- Du, P., & Wang, J.-M. 2019, *ApJ*, **886**, 42
- Du, P., Hu, C., Lu, K.-X., et al. 2014, *ApJ*, **782**, 45
- Du, P., Hu, C., Lu, K.-X., et al. 2015, *ApJ*, **806**, 22
- Du, P., Zhang, Z.-X., Wang, K., et al. 2018, *ApJ*, **856**, 6
- Ferguson, J. W., Korista, K. T., & Ferland, G. J. 1997, *ApJS*, **110**, 287
- Ferland, G. J., Done, C., Jin, C., Landt, H., & Ward, M. J. 2020, *MNRAS*, **494**, 5917

- Ferland, G. J., Chatzikos, M., Guzmán, F., et al. 2017, *RMxAA*, **53**, 385
- Fonseca Alvarez, G., Trump, J. R., Homayouni, Y., et al. 2020, *ApJ*, **899**, 73
- Green, P. J. 1996, *ApJ*, **467**, 61
- Grier, C. J., Trump, J. R., Shen, Y., et al. 2017, *ApJ*, **851**, 21
- Grier, C. J., Shen, Y., Horne, K., et al. 2019, *ApJ*, **887**, 38
- Guo, H., Shen, Y., & Wang, S., 2018 PyQSOFit: Python Code To Fit The Spectrum Of Quasars, Astrophysics Source Code Library, ascl:1809.008
- Guo, H., Shen, Y., He, Z., et al. 2020, *ApJ*, **888**, 58
- Ho, L. C. 2008, *ARA&A*, **46**, 475
- Homayouni, Y., Trump, J. R., Grier, C. J., et al. 2020, *ApJ*, **901**, 55
- Hoormann, J. K., Martini, P., Davis, T. M., et al. 2019, *MNRAS*, **487**, 3650
- Hu, C., Li, S.-S., Yang, S., et al. 2021, *ApJS*, **253**, 20
- Just, D. W., Brandt, W. N., Shemmer, O., et al. 2007, *ApJ*, **665**, 1004
- Kaspi, S., Brandt, W., Maoz, D., et al. 2021, *ApJ*, **915**, 129
- Kaspi, S., Brandt, W. N., Maoz, D., et al. 2007, *ApJ*, **659**, 997
- Kaspi, S., Smith, P. S., Netzer, H., et al. 2000, *ApJ*, **533**, 631
- Korista, K., Baldwin, J., Ferland, G., & Verner, D. 1997, *ApJS*, **108**, 401
- Korista, K. T., & Goad, M. R. 2000, *ApJ*, **536**, 284
- Korista, K. T., & Goad, M. R. 2004, *ApJ*, **606**, 749
- Korista, K. T., & Goad, M. R. 2019, *MNRAS*, **489**, 5284
- Kubota, A., & Done, C. 2018, *MNRAS*, **480**, 1247
- Kynoch, D., Mitchell, J. A. J., Ward, M. J., et al. 2023, *MNRAS*, **520**, 2781
- Leighly, K. M. 2004, *ApJ*, **611**, 125
- Li, I.-H., J., Shen, Y., Brandt, W. N., et al. 2019, *ApJ*, **884**, 119
- Lira, P., Kaspi, S., Netzer, H., et al. 2018, *ApJ*, **865**, 56
- Luo, B., Brandt, W. N., Hall, P. B., et al. 2015, *ApJ*, **805**, 122
- Lusso, E., & Risaliti, G. 2016, *ApJ*, **819**, 154
- Maithil, J., Brotherton, M. S., Shemmer, O., et al. 2022, *MNRAS*, **515**, 491
- Malik, U., Sharp, R., Penton, A., et al. 2023, *MNRAS*, **520**, 2009
- Martinez-Aldama, M. L., Czerny, B., Kawka, D., et al. 2019, *ApJ*, **883**, 170
- Mathews, W. G., & Ferland, G. J. 1987, *ApJ*, **323**, 456
- Matsuoka, Y., Kawara, K., & Oyabu, S. 2008, *ApJ*, **673**, 62
- Mitchell, J. A. J., Done, C., Ward, M. J., et al. 2023, *MNRAS*, **524**, 1796
- Negrete, C. A., Dultzin, D., Marziani, P., & Sulentic, J. W. 2012, *ApJ*, **757**, 62
- Ni, Q., Brandt, W. N., Luo, B., et al. 2018, *MNRAS*, **480**, 5184
- Ni, Q., Brandt, W. N., Luo, B., et al. 2022, *MNRAS*, **511**, 5251
- Panda, S., Czerny, B., Done, C., & Kubota, A. 2019, *ApJ*, **875**, 133
- Peterson, B. M. 1993, *PASP*, **105**, 247
- Peterson, B. M., Wanders, I., Bertram, R., et al. 1998, *ApJ*, **501**, 82
- Peterson, B. M., Berlind, P., Bertram, R., et al. 2002, *ApJ*, **581**, 197
- Peterson, B. M., Ferrarese, L., Gilbert, K. M., et al. 2004, *ApJ*, **613**, 682
- Petrucci, P. O., Ursini, F., De Rosa, A., et al. 2018, *A&A*, **611**, A59
- Plotkin, R. M., Shemmer, O., Trakhtenbrot, B., et al. 2015, *ApJ*, **805**, 123
- Reynolds, C. S. 2021, *ARA&A*, **59**, 117
- Richards, G. T., Lacy, M., Storrie-Lombardi, L. J., et al. 2006, *ApJS*, **166**, 470
- Shakura, N. I., & Sunyaev, R. A. 1973, *A&A*, **24**, 337
- Shen, Y. 2013, *BASI*, **41**, 61
- Shen, Y., & Ho, L. C. 2014, *Natur*, **513**, 210
- Shen, Y., Richards, G. T., Strauss, M. A., et al. 2011, *ApJS*, **194**, 45
- Shen, Y., Brandt, W. N., Dawson, K. S., et al. 2015a, *ApJS*, **216**, 4
- Shen, Y., Greene, J. E., Ho, L. C., et al. 2015b, *ApJ*, **805**, 96
- Shen, Y., Hall, P. B., Horne, K., et al. 2019, *ApJS*, **241**, 34
- Shen, Y., Grier, C. J., Horne, K., et al. 2024, *ApJS*, **272**, 26
- Sigut, T. A. A., & Pradhan, A. K. 2003, *ApJS*, **145**, 15
- Steffen, A. T., Strateva, I., Brandt, W. N., et al. 2006, *AJ*, **131**, 2826
- Temple, M. J., Matthews, J. H., Hewett, P. C., et al. 2023, *MNRAS*, **523**, 646
- Timlin, J. D. I., Brandt, W. N., & Laor, A. 2021, *MNRAS*, **504**, 5556
- Timlin, J. D., Brandt, W. N., Ni, Q., et al. 2020, *MNRAS*, **492**, 719
- U, V., Barth, A. J., Vogler, H. A., et al. 2022, *ApJ*, **925**, 52
- Vestergaard, M., & Peterson, B. M. 2006, *ApJ*, **641**, 689
- Wang, J.-M., Du, P., Li, Y.-R., et al. 2014a, *ApJL*, **792**, L13
- Wang, J.-M., Qiu, J., Du, P., & Ho, L. C. 2014b, *ApJ*, **797**, 65
- Wang, S., & Woo, J.-H. 2024, *ApJS*, **275**, 13
- Watson, D., Denney, K. D., Vestergaard, M., & Davis, T. M. 2011, *ApJL*, **740**, L49
- Woo, J.-H., Yoon, Y., Park, S., Park, D., & Kim, S. C. 2015, *ApJ*, **801**, 38
- Woo, J.-H., Wang, S., Rakshit, S., et al. 2024, *ApJ*, **962**, 67
- Wu, J., Brandt, W. N., Anderson, S. F., et al. 2012, *ApJ*, **747**, 10
- Wu, J., Brandt, W. N., Hall, P. B., et al. 2011, *ApJ*, **736**, 28
- Wu, Q., & Shen, Y. 2022, *ApJS*, **263**, 42
- Yu, L.-M., Zhao, B.-X., Bian, W.-H., Wang, C., & Ge, X. 2020, *MNRAS*, **491**, 5881
- Yu, Z., Martini, P., Penton, A., et al. 2021, *MNRAS*, **507**, 3771
- Yu, Z., Martini, P., Penton, A., et al. 2023, *MNRAS*, **522**, 4132
- Yuan, F., & Narayan, R. 2014, *ARA&A*, **52**, 529